International Journal of Mechanical Sciences 287 (2025) 109979

Contents lists available at ScienceDirect

International Journal of Mechanical Sciences

journal homepage: www.elsevier.com/locate/ijmecsci

Short-range ordering suppresses mechanical annealing in CoCrNi alloy nanopillars

Luling Wang [a,1], Chi Xu [b,d,1], Binpeng Zhu [a], Jizi Liu [a], Ningning Liang [a], Runchang Liu [a], Yang Cao [a,c,*], Yonghao Zhao [a,c,*]

[a] Nano and Heterogeneous Materials Center, School of Materials Science and Engineering, Nanjing University of Science and Technology, Nanjing 210094, China
[b] College of Mechanical Engineering, Yancheng Institute of Technology, Yancheng, 224051, China
[c] School of Materials Science and Engineering, Hohai University, Changzhou, 213200, China
[d] College of Mechanical and Electrical Engineering, Nanjing University of Aeronautics and Astronautics, Nanjing 210016, China

ARTICLE INFO

Keywords:
Molecular dynamics
Single crystalline nanopillars
Medium-entropy alloy
Mechanical annealing
Local Peierls friction force
Chemical short-range order

ABSTRACT

Comprehensive atomic simulations have been conducted to compare the effects of pre-existing dislocation densities on the intermittent plastic behaviors of CoCrNi medium-entropy alloy (MEA) single-crystalline nanopillars with that of pure metal nanopillars. In contrast to pure metal nanopillars that demonstrate prolonged nearly elastic loading and reloading segments, the MEA nanopillars show short loading and reloading segments and high dislocation densities throughout the entire deformation process, suggesting that mechanical annealing is substantially suppressed in MEA nanopillars. The closely spaced junctions between the short-range-order domains and adjacent Ni clusters exert exceptionally strong local Peierls friction forces that not only slow down dislocation slip, but also increase the probability for dislocation entanglement. As a result, high densities of dislocations can be accumulated during the plastic deformation of the MEA nanopillars, leading to suppression of mechanical annealing and transition from exhaustion hardening to strain hardening. This work provides new insights to the plastic deformation of MEA nanopillars that are distinctive from pure metal nanopillars.

1. Introduction

The research on the mechanical behaviors and deformation mechanisms of nanopillars has gained tremendous momentum since the beginning of the new millennium [1,2], in support of the fast development of nanotechnology [3,4] and scaling-down of micro-electro-mechanical systems [5]. After 20 years of research and development, we have realized that there are strict scaling laws governing the stress-strain responses of nanopillars, including size-dependent dislocation nucleation [6–8], size-dependent crystal flow [9] and strain-rate dependent plasticity [10–12]. All these scaling laws relate to the very high surface-to-volume ratio [10,11,13], very small volume and limited dislocation storage capacity (dislocation density) [2,11]. Apparently, high surface-to-volume ratio and minuscule volume are the geometry characteristic of nanopillars, and thus cannot be changed with much freedom. The only factor with a large adjustable range seems to be the dislocation storage capacity. For nanopillars made of pure metals or dilute solid solutions (most of the conventional alloys), on one hand the plastic flow is confined in a very small volume having the short axis of only a few tens or hundreds of nanometers; On the other hand, the forces exerted by lattice friction, solute pinning and dislocation entanglement, are insufficient to counterbalance the combined effect of image force [2], shear stress and repulsive force (between dislocations) [14]; Therefore, dislocations (plastic strain carriers) can easily escape from the pillar surface [15], resulting in mechanical annealing [2] and dislocation starvation [16]. From this point of view, the dislocation storage capacity is also limited in the nanopillars. So, is this the end of the road?

In recent years, high- and medium-entropy alloys (HEAs and MEAs), which are concentrated solid solutions, have received tremendous attention from both scientific and engineering communities, because of the vastly adjustable atomic configurations [17,18] and excellent low temperature mechanical properties [19]. Provided that enthalpic interactions favor chemical affinity of elemental pairs in concentrated

* Corresponding authors at: Nano and Heterogeneous Materials Center, School of Materials Science and Engineering, Nanjing University of Science and Technology, Nanjing 210094, China.
E-mail addresses: y.cao@njust.edu.cn (Y. Cao), yhzhao@njust.edu.cn (Y. Zhao).
[1] These authors contributed equally to this work.

https://doi.org/10.1016/j.ijmecsci.2025.109979
Received 20 September 2024; Received in revised form 13 January 2025; Accepted 13 January 2025
Available online 16 January 2025

solid solutions [20–25], the scenario of the ideal random solid solution [26–30] is insufficient to describe HEAs and MEAs. In fact, the characteristic multi-principal element design grants the possibility of having different atomic configurations such as random elemental distribution, chemical short-range ordering (SRO) [17,18,20,31–37], segregation, clustering [38–41] and incipient concentration waves [17,42] in HEAs and MEAs without changing the bulk compositions. By adjusting the atomic configurations, it is possible to elevate the dislocation storage capacity to a very high level [43–45], and thus to stimulate a superior forest hardening effect in a solid solution [46,47].

While it is known that the mean-field conditions for forest hardening breaks down in minuscule volumes [9], we would not expect substantial forest hardening in nanopillars. However, considering the high dislocation storage capacity and the strong dislocation pinning effects from local atomic configurations, we wonder if at least the dislocation starvation [2] can be suppressed in the nanopillars of concentrated solid solutions. Moreover, when a very high density of dislocations comes to play in the deformation of a nanopillar, can the plastic flow be different from the conventional metallic nanopillars.

In this work, we use atomistic models that mimic the plastic deformation of CoCrNi MEA nanopillars with varied local chemical orders and vastly varied densities of pre-existing dislocations, to demonstrate that the usually observed mechanical annealing can be suppressed by the strong local Peierls friction forces associated with chemical short-range ordering. Moreover, dislocation entanglement and accumulations have been observed in the CoCrNi MEA nanopillar with SRO, showing for the first time the sign of strain hardening in the single-crystalline nanopillar with the diagonal length of only a few tens of nanometers.

The remaining sections of this work are organized as follows: Section 2 details the molecular dynamics (MD) simulation methods. Section 3 presents the results, starting with the uniaxial compression responses of single crystalline nanopillars and the associated dislocation activities; then, the physical origin of the high dislocation storage capacity of CoCrNi nanopillars is revealed by explicating the local Peierls friction forces; in addition, the unexpected strain hardening in CoCrNi nanopillars is revealed. In Section 4, the mechanical annealing behaviors in pure metal and CoCrNi nanopillars are compared and discussed, based on our simulation results and experimental evidences from literatures; furthermore, the fundamental mechanism underlying the transition from exhaustion hardening to strain hardening in CoCrNi nanopillars is discussed in detail. In Section 5, main conclusions are drawn to tie together the key findings and main arguments.

2. Methodology

In this section, the modeling of nanopillars with pre-existing dislocations is presented; The definition and calculation of the SRO parameter are elaborated; The calculation procedure for the local Peierls friction force based on the interatomic potential is provided and clarified in detail.

2.1. Modeling and MC/MD simulation

In this work, all atomistic simulations were performed based on the LAMMPS code [48]. The density functional theory (DFT)-calibrated embedded atom method (EAM) potential developed by Li et al. [18] was used to study the mechanical annealing behaviors of the CoCrNi and Ni single-crystalline nanopillars. Compared with the experimental and DFT calculation results [34,49], this potential can be used for predicting materials properties such as lattice constant, unstable and stable stacking fault energies (SFEs) with confidence. Four sets of nanopillars with a consistent size of $20\times20\times30$ nm^3 were made: (1) random solid solution (RSS) CoCrNi, (2) CoCrNi alloy with SRO, (3) pure Ni and (4) pure Cu [50]. The RSS nanopillars were constructed in the ATOMSK program with random substitutions of atoms of different species [51]. Then, the SRO nanopillars were obtained by the hybrid Monte Carlo (MC) and MD methods [52,53]. For MC trials, chemical potential differences $\Delta\mu_{NiCo}$ and $\Delta\mu_{NiCr}$ were set as 0.021 and -0.31 eV, respectively. The variance parameter κ was set to be 1000. Hybrid MC/MD relaxation with N/4 times (N is the number of atoms) of trial swaps every 0.05 ps for a total of 80000 cycles was performed, and each model was relaxed at 300 K using NPT ensemble [54]. The typical RSS and SRO models are shown in Fig. 1a and b, respectively. The chemical short-range order parameter proposed by Fontaine [55] was used to define the degree of ordering at the first nearest neighbor: $\alpha_{ij} = 1 - P_{ij}/C_j$ $(i \neq j)$ and $\alpha_{ii} = P_{ii} - C_i/(1- C_i)$, where α_{ij} represents the chemical short-range order parameter between i-type and j-type atoms; P_{ij} is the probability of finding a j-type atom near an i-type atom; C_i and C_j denote the average concentrations of i-type and j-type atoms, respectively. Fig. 1c presents the chemical short-range order parameter α_{ij} at the first nearest neighbor. For the RSS system, all α_{ij} are close to zero, demonstrating the random distribution of three principal elements. For the SRO systems, positive α_{NiNi} indicates the presence of Ni segregation while negative α_{CoCr} represent local Co-Cr ordering.

The bulk properties and defect properties of the materials were calculated by Molecular statics (MS) simulation and are presented in Table 1. The nanopillars in the initial states were obtained by manually inserting full dislocation loops and subsequently annealing at 300 K for 300 ps via the NPT ensemble, as shown in Fig. 2. Specifically, a total of 36 full dislocation loops were inserted into four unparallel {111} planes to obtain different initial dislocation densities ($10^{15} \sim 10^{17}$ m^{-2}). The radii of the dislocation loops were set to 30~70 Å. The dislocation loops are non-overlapping and randomly distributed on atomic planes. The manually inserted full dislocation loops would undergo stochastic mutual trapping and escaping processes until a thermal equilibrium was reached (Fig. 2a and b). Therefore, the desired densities of pre-existing dislocations can only be obtained after multiple trials. Fig. 2c shows the local dislocations in the thermally balanced nanopillars, including single dislocation loop (I and II) and entangled complex dislocation configurations (III and IV), which are comparable to the defective pillars in the experiments [56]. It is noteworthy that the full dislocation loops were inserted after the MC/MD simulations, which hence affected the degree of SRO. Fig. 1c shows short-range order parameters α_{ij} for typical SRO nanopillars with different initial dislocation densities ($\rho_{initial}$), and Fig. 1d shows the corresponding dislocation networks. In this case (Fig. 1c), the perfect SRO nanopillar exhibits the highest degrees (α_{ij}) of Co-Cr ordering and Ni segregation; As the dislocation density increases to $\rho_{initial} = 2.39 \times 10^{15}$ m^{-2} and further to $\rho_{initial} = 1.06 \times 10^{17}$ m^{-2}, all α_{ij} decrease. However, the α_{ij} of Co-Cr ordering and Ni segregation remained at high levels, for which the values of α_{CoCr} and α_{NiNi} were reduced by only 0.027 and 0.01, respectively, with respect to the perfect nanopillar (Fig. 1c). This is because the damage to SRO by dislocation slip was small during the relaxion process.

2.2. Uniaxial compression simulation and data analysis

Uniaxial compressive loads along the [111] directions were applied to all single-crystalline nanopillars (Fig. 2b). This orientation has a low Schmid factor and therefore is considered the “hard orientation”, which shows large rise and fall of stresses during the exhaustion hardening and dislocation avalanche, respectively [57,58]. The four surfaces parallel to the loading direction were set as free boundaries in each pillar. The samples were compressed with a constant strain rate of 1×10^8 s^{-1}. During loading, all samples were kept at the constant temperature of 300 K via the NVT ensemble. The stress was obtained by averaging the virial compressive stresses of all atoms in the samples. Post-processing was done based on the modules performed in OVITO [59]. The information of dislocation lines was extracted by the dislocation extraction algorithm (DXA) [60,61], the method that allows us to identify the types of dislocations and obtain the number of dislocation junctions. The von Mises atomic shear strain was calculated based on the method developed by

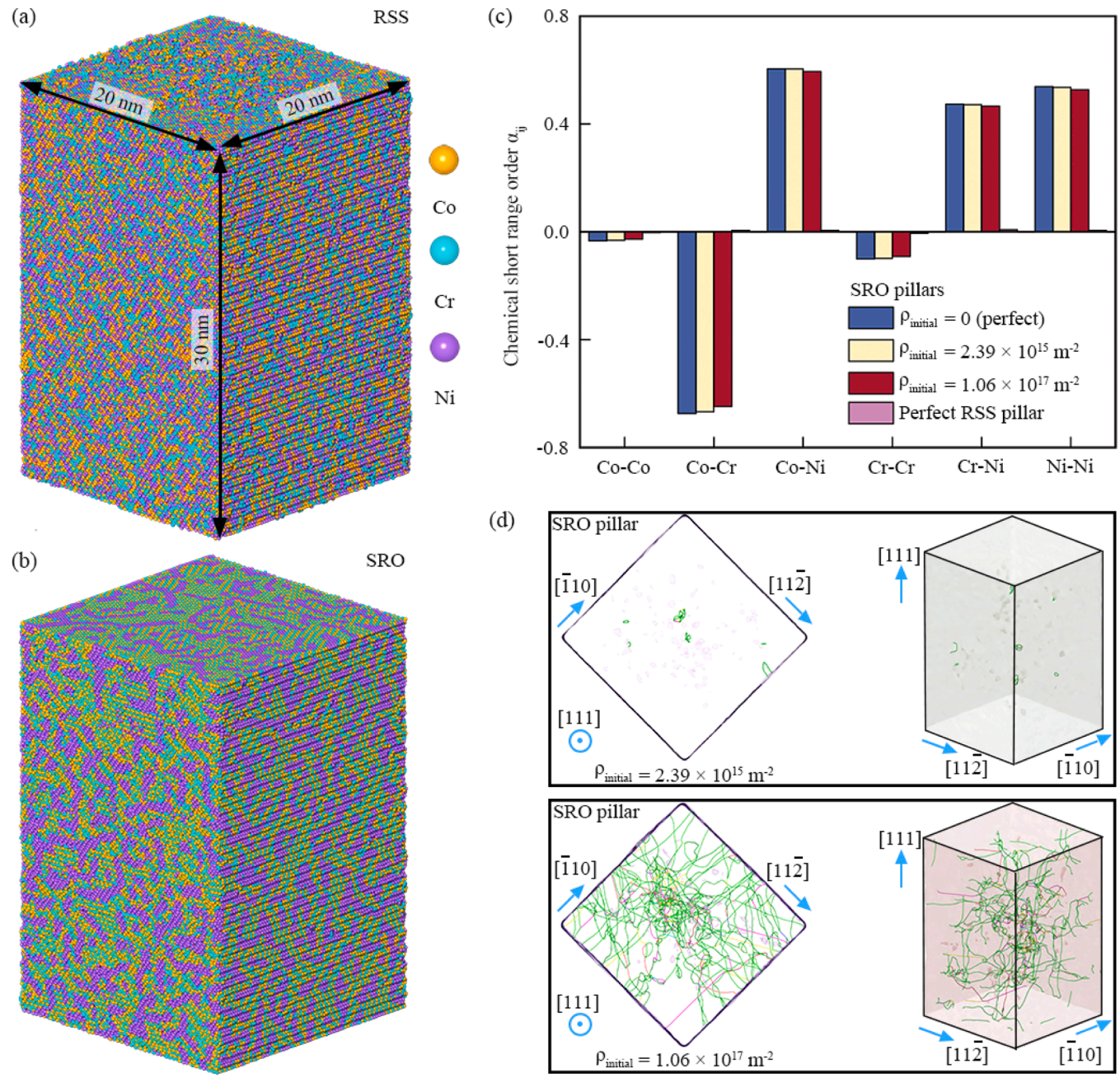

Fig. 1. Atomic configurations of single-crystalline MEA nanopillars: (a) RSS and (b) SRO pillars; (c) The chemical short-range order parameters α_{ij} of the RSS/SRO nanopillars with different initial dislocation densities $\rho_{initial}$ at the first nearest neighbors. (d) Dislocation networks in the defective SRO nanopillars corresponding to (c).

Shimizu et al. [62].

2.3. Calculation for the local Peierls friction force F_P

An example for the calculation of the local Peierls friction force (F_P) in the RSS system is given as steps 1 to 4 (the same procedure was applied to the SRO system):

Step 1: Plot the cohesive energy vs. lattice constant curve to obtain the equilibrium lattice constant (corresponding to the lowest energy) for the target system at 0 K, as shown in Fig. 3a. Use the equilibrium lattice constant to construct a single crystal sample, as shown in Fig. 3b.

Step 2: The crystal model was divided into two parts, the 'Upper' and 'Lower' parts, by the {111} generalized stacking fault (GSF) plane, as shown in Fig. 3b. While the lower part was kept still, serial displacements (δx, δy) of the upper part were done in the [10$\bar{1}$] and [$\bar{1}$2$\bar{1}$] directions with energy minimization after per displacement. In order to obtain a smooth atomic energy landscape in post processing, it is recommended to use '*fix setforce*' and '*fix aveforce*' commands during energy minimization, so that the forces acting on the atoms in [10$\bar{1}$] and [$\bar{1}$2$\bar{1}$] directions are set to 0, while the forces acting in [111] direction are distributed equally per atom. Simulation boxes were energy-minimized by using the fire algorithm [63] with energy and force tolerances of 10^{-12} eV and 10^{-14} eV/Å, respectively. Periodic boundary conditions were enforced in the [10$\bar{1}$] and [$\bar{1}$2$\bar{1}$] directions, and the non-periodic boundary condition was enforced in the [111] direction.

Step 3: The potential energy of each atom on the GSF plane after displacements (δx, δy) was extracted and stored using a Python script. Then, the GSF energy landscape for each atom was interpolated using

Table 1
Calculated bulk and defect properties of CoCrNi, pure Ni and Cu using EAM potentials developed by Li et al. [18] and Mishin et al. [50]. The lattice constant a, cohesive energy E_{coh}, elastic constants C_{11}, C_{12}, and C_{44}, shear modulus G, stable stacking fault energy γ_{isf} and unstable stacking fault energy γ_{usf} are included.

	RSS	SRO	Ni	Cu
a (Å)	3.556	3.560	3.52	3.615
E_{coh} (eV/atom)	-4.32	-4.41	-4.45	-3.54
C_{11} (GPa)	251.5	267	262	170
C_{12} (GPa)	179	198	155	122
C_{44} (GPa)	95.2	100	122	76
G (GPa)	64.65	65.32	87.63	47.95
γ_{isf} (mJ/m^2)	~-18	~60	125	44
γ_{usf} (mJ/m^2)	~312	~342	366	161

cubic splines to generate smooth paths, as exemplified in Fig. 3c.

Step 4: Three local minima points (points i, ii and iii in Fig. 3c) on the GSF energy landscape were extracted by using the BFGS algorithm [64]. Then, the GSF energy along the path i→ii→iii was plotted as the orange line in Fig. 3d. Finally, the local Peierls friction forces (Fig. 3d) experienced by the leading and trailing dislocations can be obtained by finding the highest slopes on the GSF energy profile.

3. Results

In this section, mechanical annealing in pure metal and CoCrNi alloy nanopillars are studied based on uniaxial compression responses and dislocation activities. Suppression of mechanical annealing in CoCrNi nanopillars is revealed, and explained based on the analysis of local Peierls friction forces; Finally, transitions from exhaustion hardening to strain hardening in SRO CoCrNi nanopillars during plastic deformation are revealed.

3.1. Elastic and plastic strain in nanopillar deformation

Figs. 4a-d show the stress-strain responses for the single-crystalline nanopillars with different densities of pre-existing dislocations subjected to uniaxial compression. The densities of pre-existing dislocations were varied but below 5×10^{15} m^{-2}, which are comparable to the dislocation densities found in experimental results [2,65–67]. All nanopillars show multiple stress drops and subsequent reloading segments during compressive plastic deformation, resulting in the zig-zag shape stress-strain curves as shown in Fig. 4a–d, despite of different compositions and chemical ordering. For the RSS CoCrNi pillars as shown in Fig. 4a, the initial yielding stresses are approximately 6.5–7.4 GPa which are very close to the highest stresses of ~7.2–8.0 GPa attained at some of the reloading peaks during the compressive deformation after yielding. At the end of each stress drop (it is also the starting point of each reloading segment), the stress dropped significantly to ~2.0–3.5 GPa. For the SRO CoCrNi pillars as shown in Fig. 4b, the initial yielding stresses are in the range of ~8.2–9.6 GPa which are significantly higher than that of the RSS CoCrNi pillars, despite of the same overall chemical composition. It is worth to note that the highest stresses of the SRO CoCrNi pillars during the plastic deformation stage never exceed the yield stresses, indirectly showing the "glide plane softening" effect [20–22].

To clarify the "glide plane softening" effect, the GSF energy curves for atomic displacements along (111) $<11\bar{2}>$ in the SRO and RSS models were calculated. The models with the size of 7.56 × 8.73 × 9.26 nm^3 were built on the $[1\bar{1}0]$-x, $[11\bar{2}]$-y and [111]-z coordinate system. The GSF energy curves were obtained by displacing one half of the crystal along a (111) surface in the $[11\bar{2}]$-y-direction with subsequent energy minimization. Periodic boundary conditions were applied in both x- and y-directions, while the atoms were allowed to relax along z-direction. Since it is impossible to accurately perform rigid displacements along the directions of a leading partial dislocation and a trailing partial dislocation (two non-perpendicular directions) in the same

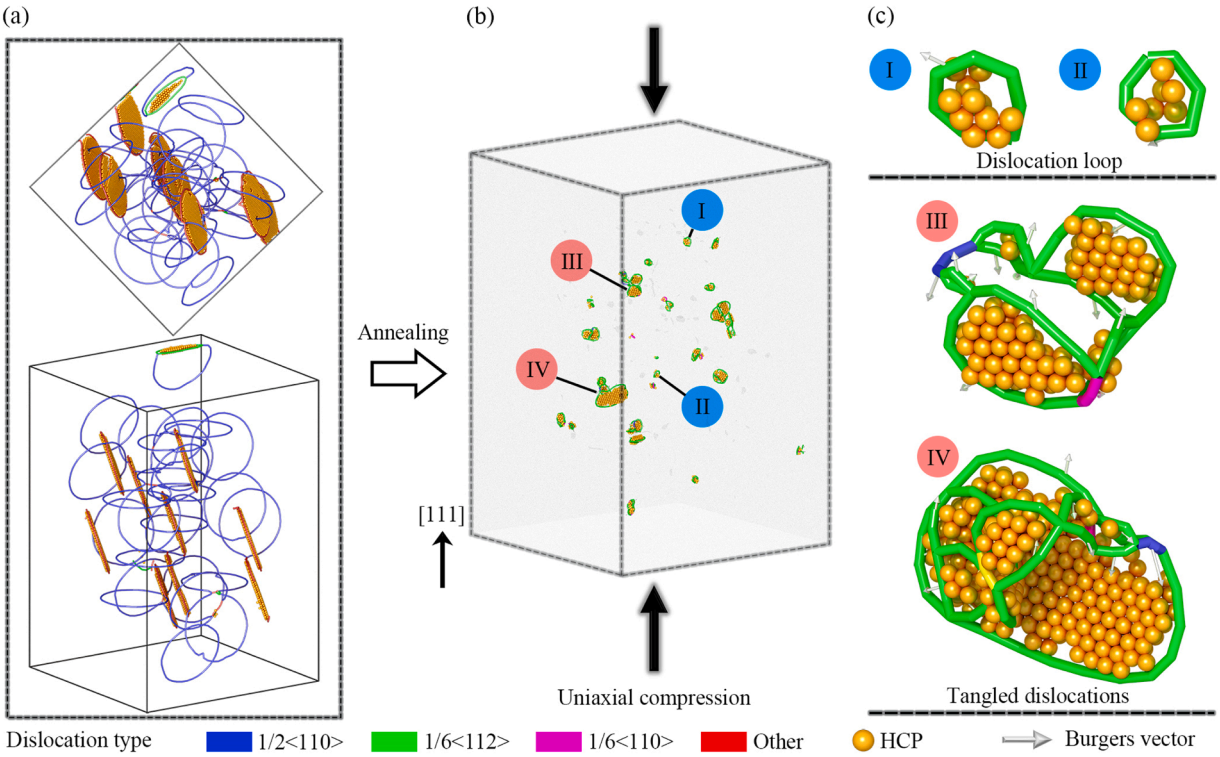

Fig. 2. Modeling of nanopillars containing pre-existing dislocations. (a) A single-crystalline nanopillar containing manually inserted dislocation loops; (b) The annealed nanopillar containing pre-existing dislocations; (c) Enlarged views of dislocation structures in (b).

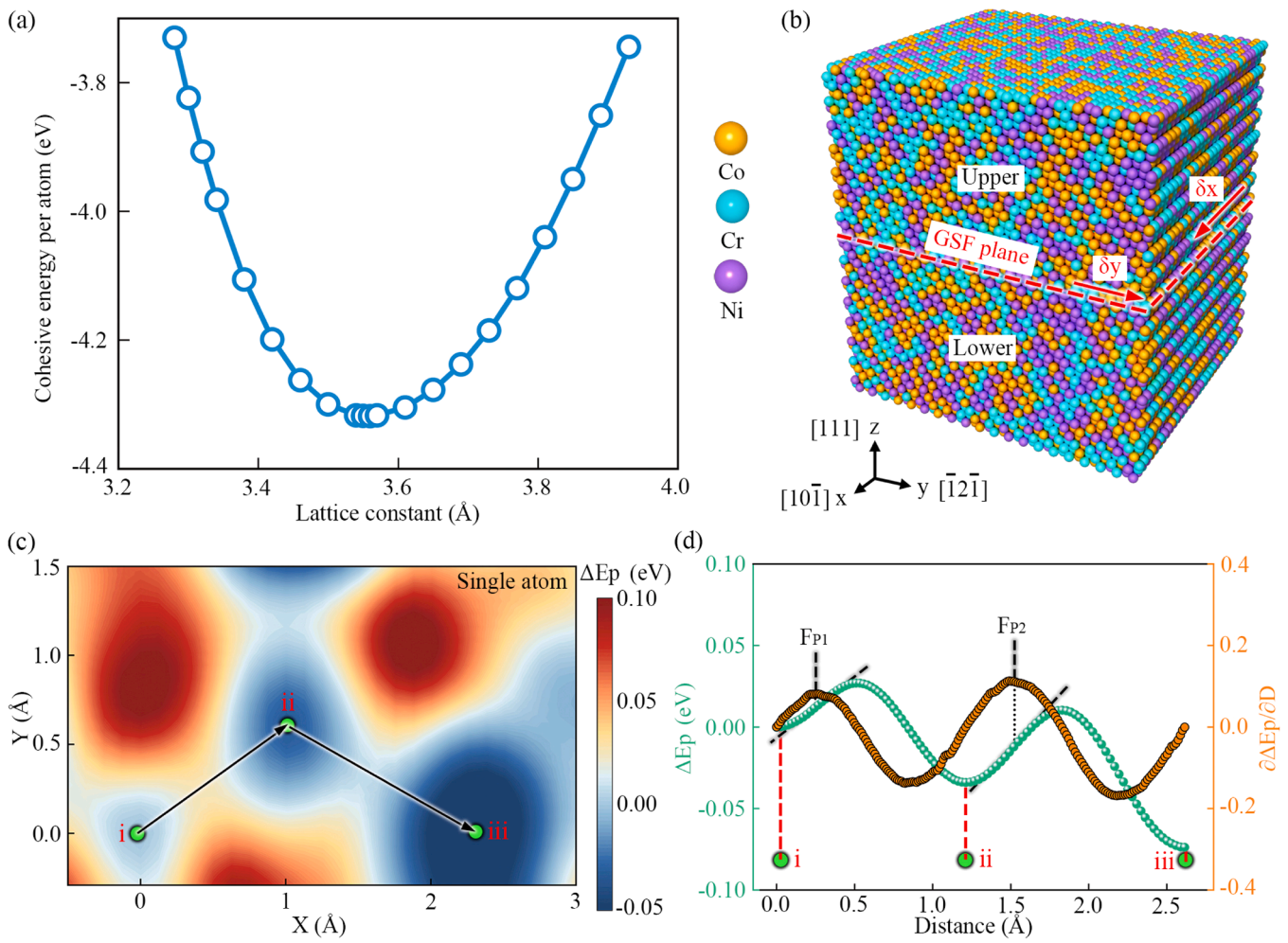

Fig. 3. Calculation example of the local Peierls friction force. (a) Cohesive energy vs. lattice constant for the equimolar CoCrNi MEA at 0 K (the lowest energy corresponds to the equilibrium lattice constant). (b) The crystal model built for calculating the GSF energy. (c) The local GSF energy landscape resolved for the displacement of a single atom along the path i→ii→iii. (d) The local GSF energy profile (green line) and its gradients (orange line) along the path i→ii→iii in (c).

configuration, we will only investigate the energy barriers related to the leading partial dislocation. Fig. 5a and b show GSF energy curves for the SRO and RSS models, respectively. The unstable stacking fault energy E^i_{usf} is thus equal to the energy barrier $\Delta E^1_{barrier}$ for the formation of a leading partial dislocation in the SRO or RSS structure. $\Delta E^2_{barrier}$ and $\Delta E^3_{barrier}$ are the energy barriers for the formation of leading partial dislocations on the same slip plane in the subsequent two slip periods, as shown in Figs. 5a and b. $\Delta E^i_{final}(i=1,\ 2,\ 3)$ is the energy of the atom in the equilibrium position after completing the unit displacement, $\frac{\sqrt{6}}{6}a$. Sequential cross-sectional snapshots on a selected $(1\bar{1}0)$ plane in the SRO model are shown in Fig. 5c–h, corresponding to the points labelled c-h in Fig. 5a. The top half of the model is displaced in the $[11\bar{2}]$-y-direction, resulting in the sequential change of atomic arrangements on the displaced (111) plane. Due to the relative sliding of the upper half of the crystal, the atoms on the two adjacent (111) planes deviated from the original face-centered-cubic (FCC) structure (colored in green) and were identified by common neighbor analysis as the unknown type (the white atoms).

GSF energy calculation has been repeated ten times for both SRO and RSS structures for statistical analysis. The results are shown in Fig. 5i. By comparing the orange bars at the positions 1, 2 and 3 on Fig. 5i, it can be seen that $\Delta E^1_{barrier}$ is about 33 ~ 38 mJ/m^2 larger than $\Delta E^2_{barrier}$ and $\Delta E^3_{barrier}$; This result indicates that once a leading partial dislocation has glided across the (111) plane, the energy barrier for the subsequent leading partial dislocation slip is reduced due to the destruction of SRO. The heights of the orange bars at the positions 2 and 3 are similar to the heights of the purple bars at the positions 1, 2 and 3; This comparison result indicates: (1) Once the SRO is destroyed by the first leading partial dislocation, the energy barriers for the following leading partial dislocation slip are reduced to the level similar to that in the RSS structure; (2) The first leading partial dislocation slip does negligible change to the energy barrier for subsequent dislocation slip in the RSS structure. Moreover, the intrinsic stacking fault energies $E^i_{isf}\ (i=1,\ 2,\ 3) \widehat{=} \Delta E^i_{final}$ of the SRO structure also decreased from ~58 mJ/m^2 at position 1 to -22 and -26 mJ/m^2 at positions 2 and 3, respectively. This result indicates that dislocation slip in an SRO structure also changes the SFEs on the slip planes. The quantitative analysis also shows that the short-range order parameters α_{ij} of the five typical SRO nanopillars (Fig. 4b) will continue decreasing during plastic deformation, as shown in Supplementary information S1. To sum up, planar slip in the SRO structure can cause plane softening by reducing the energy barrier for dislocation slip.

Once the initial yielding and subsequent stress drop occurred, the dislocation avalanche broke down the initial state of SRO, hence the stress was lowered for successive stress drops. The lowest stresses attained at the ends of stress drops for the SRO CoCrNi nanopillars were ~2.8–3.3 GPa which were very much comparable to the RSS CoCrNi nanopillars. For comparison purposes, the stress-strain responses of Ni and Cu nanopillars are provided in Fig. 4c and d, respectively. For all Ni nanopillars and the Cu nanopillars 1, 2, and 3, the highest stresses were

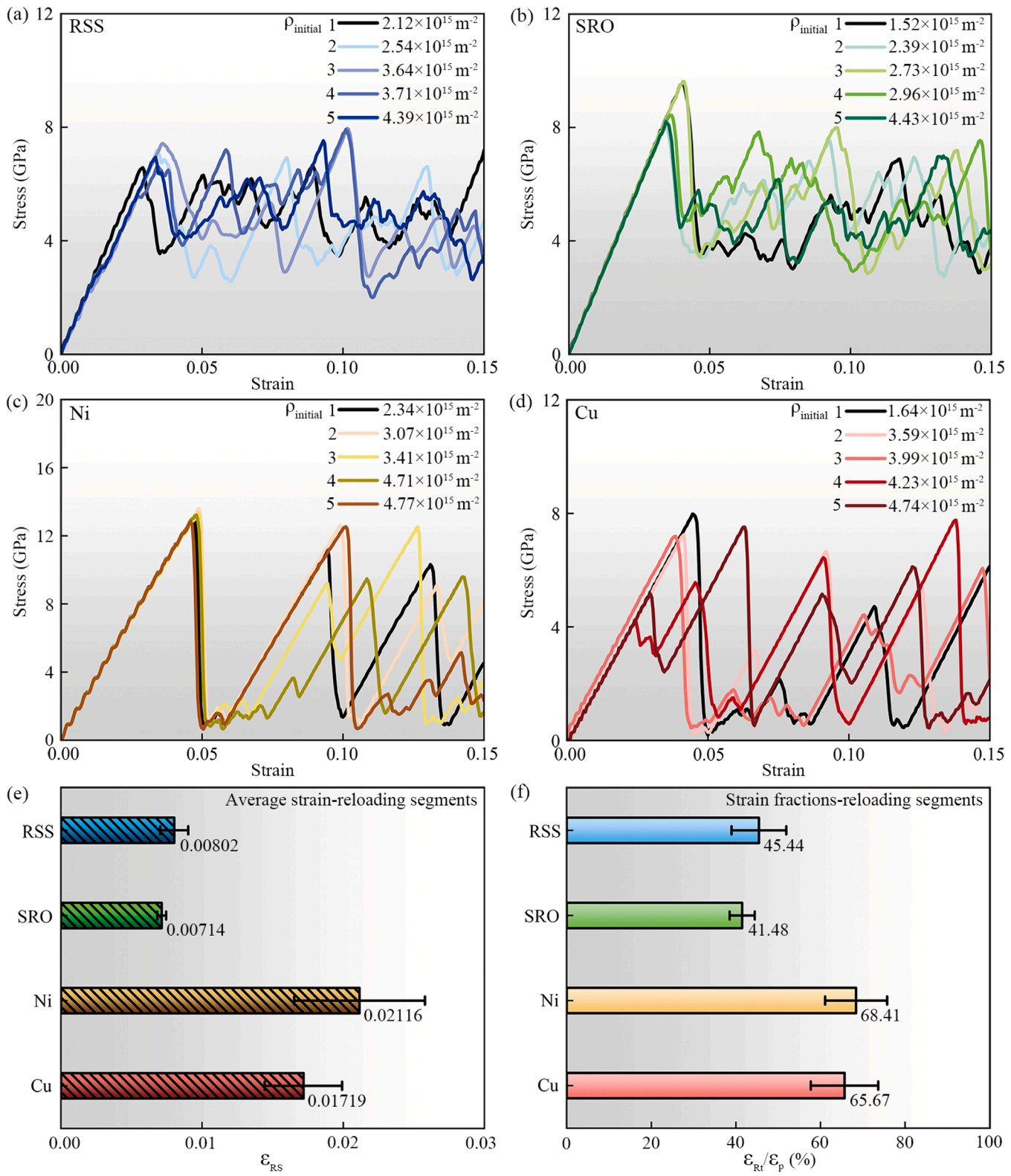

Fig. 4. Compressive stress-strain curves for the nanopillars containing different initial dislocation densities: (a) RSS CoCrNi MEA nanopillars; (b) SRO CoCrNi MEA nanopillars; (c) pure Ni nanopillars; (d) pure Cu nanopillars. ($\rho_{initial}$ is the density of pre-existing dislocations in a nanopillar.) (e) Comparison of average strain per reloading segment. (f) The fraction of total strain contributed by reloading segments. (The error bars represent the standard deviations among the set of five curves).

all recorded at the initial yielding points. During the compressive deformation, the stresses drop significantly to below 1 GPa for all Ni and Cu nanopillars after stress drops, despite that the yield stresses of Ni nanopillars are ~12.8–13.6 GPa which are significantly higher than the CoCrNi nanopillars.

After every stress drop, a nearly elastic reloading segment that demonstrates linear increase of stress with increasing strain will form until the next stress peak, as shown in Fig. 4a–d. A parameter ε_{RS} is

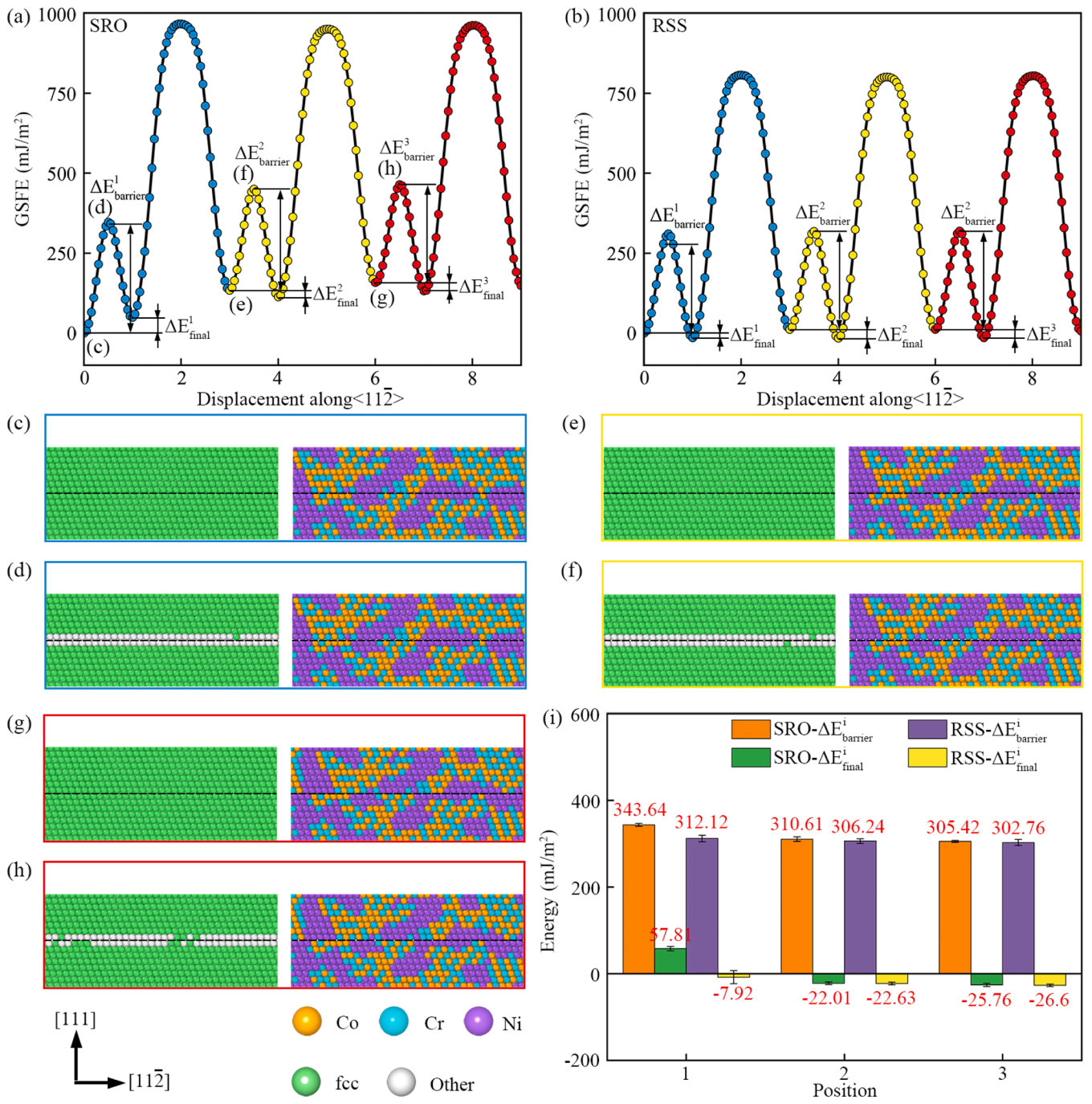

Fig. 5. Representative GSF energy curves along (111) <11$\bar{2}$>. (a) SRO and (b) RSS structures (the unit displacement is $\frac{\sqrt{6}}{6}a$). $\Delta E^i_{barrier} \widehat{=} E^i_{usf}$ $(i = 1, 2, 3)$. $\Delta E^i_{final} \widehat{=} E^i_{isf}$ $(i = 1, 2, 3)$. (c-h) Sequential cross-sectional snapshots showing the atomic structures at the corresponding positions marked (d)-(h) in (a). (i) The statistical bar chart compares $\Delta E^i_{barrier}$ and ΔE^i_{final} from total twenty SRO and RSS models. The error bars correspond to the standard deviations.

proposed here to describe the average strain attained by the reloading segments on each entire stress-strain curve, and the values of ε_{RS} are compared for all four sets of nanopillars in Fig. 4e. The ε_{RS} measured for both RSS and SRO CoCrNi nanopillars are very low in comparison to the pure metal nanopillars. The SRO CoCrNi nanopillars have the lowest ε_{RS} = 0.00714 which is three times smaller than the Ni nanopillars (ε_{RS} = 0.02116), as shown in Fig. 4e. The total strain carried by the reloading segments (ε_{Rt}) is divided by the total strain attained (ε_p) after initial yielding to reveal the fraction of strain carried by the reloading segments (the contribution of near elastic reloading strain to the total strain after yielding), and the result is shown in Fig. 4f. All nanopillars have been deformed to the same strain of 0.15, but the fractions of strain carried by the reloading segments for pure metal nanopillars and CoCrNi nanopillars are very different; Again, the SRO CoCrNi nanopillars have the lowest $\frac{\varepsilon_{Rt}}{\varepsilon_p}$ = 41.48% which is smaller than that of Ni nanopillars ($\frac{\varepsilon_{Rt}}{\varepsilon_p}$ = 68.41%) by 26.93%.

3.2. Dislocation activities and mechanical annealing

As shown in Fig. 6a–d, the dislocation densities for all four types of nanopillars stay at comparatively low levels during the nearly elastic initial loading. At the strains ~ 0.0330 - 0.0435, sharp increase in

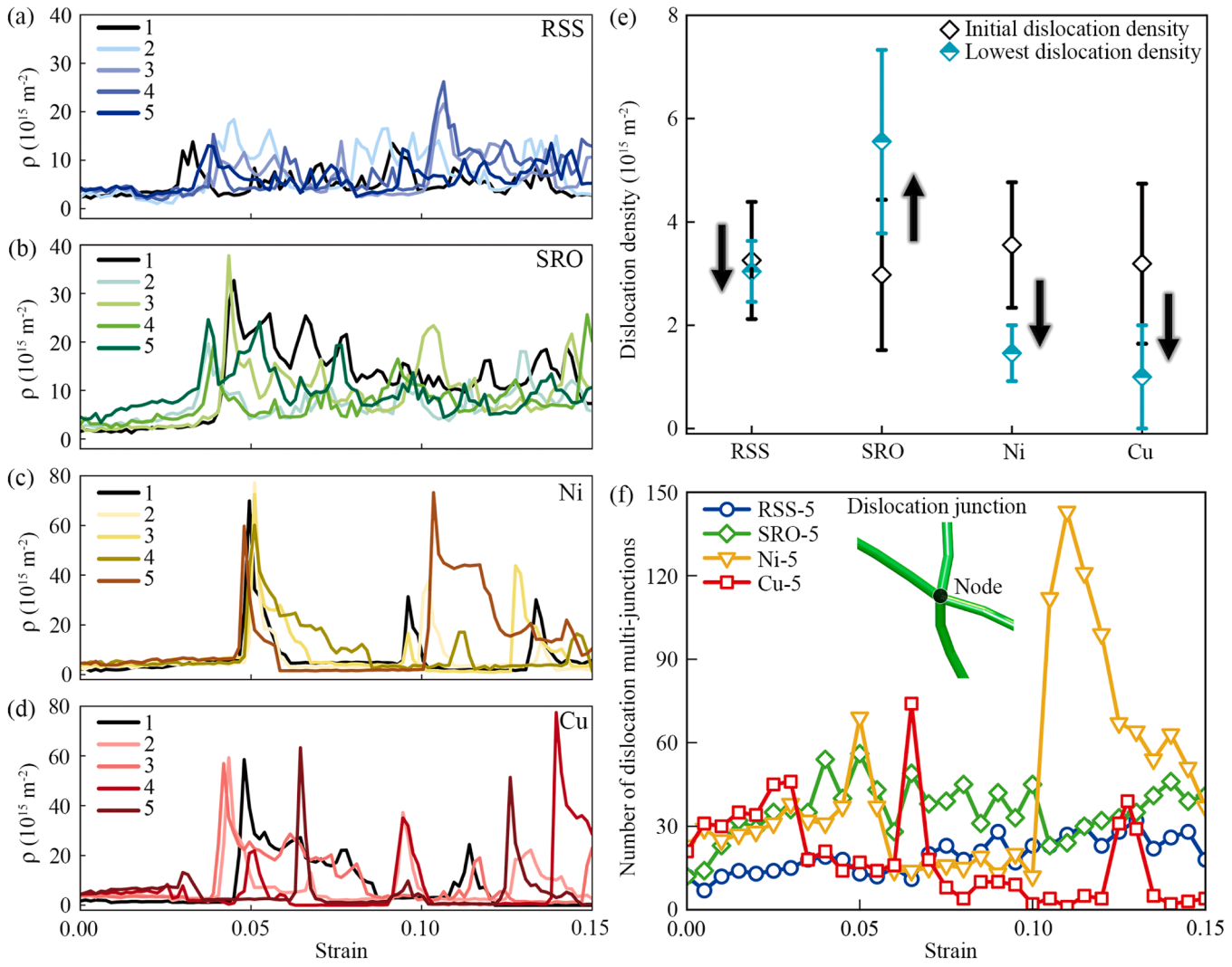

Fig. 6. Dislocation density evolutions during the plastic deformation of nanopillars. (a-d) Dislocation density evolution in RSS, SRO, pure Ni and Cu nanopillars. The result is extracted from the same 20 nanopillars analyzed in Fig. 4. (e) Comparison between the lowest dislocation densities attained during deformation (cyan diamonds) and the initial densities of pre-existing dislocations (black diamonds). The black arrows indicate the change of dislocation density with respect to the initial dislocation density. (f) Evolutions of the numbers of dislocation multi-junctions in the typical RSS, SRO, pure Ni and Cu nanopillars with similar initial dislocation densities (the fifth nanopillars in Fig. 4a–d).

dislocation densities is seen in the RSS CoCrNi nanopillars; For the SRO CoCrNi nanopillars, sharp increase in dislocation densities occurred at slightly higher strains ~ 0.0373 - 0.0450. For pure Ni and Cu nanopillars, the dislocation densities boomed at the strains ~ 0.048 - 0.051 and ~ 0.042–0.048, respectively. It is noticed that the Cu nanopillars 4 and 5 show small dislocation density peaks at strains 0.0255 and 0.03, respectively. The dislocation densities in RSS and SRO nanopillars fluctuate during plastic deformation but within the ranges of 2.45×10^{15} - 2.62×10^{16} m^{-2} and 3.78×10^{15} - 3.78×10^{16} m^{-2}, respectively; In contrast, the variation ranges of dislocation density for Ni and Cu nanopillars are 9.19×10^{14} - 7.72×10^{16} m^{-2} and 0 - 7.75×10^{16} m^{-2}, respectively.

In this simulation work, the initial dislocation densities in all four types of nanopillars are set to similar ranges (similar error bars), as shown in Fig. 6e. At the ends of stress drops, the dislocation densities in pure Ni and Cu nanopillars drop significantly to the lower end of 10^{15} m^{-2} or even zero, to demonstrate mechanical annealing [2]. However, the lowest dislocation densities in the RSS nanopillars attained at the ends of stress drops are comparable to that of the initial dislocation densities but in a smaller range of variation (a small error bar). Interestingly, the dislocation densities after stress drops in the SRO nanopillars are even increased and with a large variation range, suggesting the absence of dislocation starvation. It is noteworthy that the numbers of dislocation multi-junctions (consisting of three or more heads/tails of the dislocation lines) in the typical RSS and SRO nanopillars during deformation is relatively stable, maintaining at 7 to 32 and 12 to 56 (Fig. 6f), respectively. In contrast, the numbers of multi-junctions in pure Ni and Cu nanopillars vary considerably with intermittent exhaustion hardening and dislocation avalanche, fluctuating in the vary large ranges, 10 to 143 and 1 to 74 (Fig. 6f), respectively. Apparently, mechanical annealing has been somehow suppressed in both RSS and SRO MEA nanopillars, despite of continuous creation and decomposition of multi-junctions.

At the end of each stress drop, a large number of dislocations escaped from the nanopillar surface under the combined effect of the applied stress and image forces, leading to significant reduction of dislocation density. This phenomenon is called mechanical annealing which is common in plastically deformed nanopillars of pure metals [68,69]. However, in the current case all three types of dislocations, Shockley partial, stair-rod and Hirth-lock dislocations are reserved at the ends of stress drops, and the dislocation densities are still high in the RSS (Fig. 7a) and SRO (Fig. 7b) nanopillars. In contrast, the dislocation

densities in the pure Ni and Cu nanopillars have dropped to very low levels. Only a few Shockley partials, which are pinned by sessile stair-rod and Hirth-lock dislocations, are conserved in the Ni nanopillar, as shown in Fig. 7c. In the Cu nanopillar, there is no Shockley partial at all, as shown in Fig. 7d.

Representative dislocation slip-motion and interactions in an SRO nanopillar are shown in Fig. 7e–h. The gliding 1/6[$\bar{2}11$] Shockley dislocation shows meandering shapes, because short segments of the dislocation are intermittently pinned by some atoms (encircled by red dashed lines in Figs. 7 e and g). Note that meandering and wavy dislocation lines have been a characteristic feature in MEAs and HEAs with nanoscale chemical-order heterogeneities [18,70], which are related to compositional complexities [71]. The long meandering dislocation line glides forward to encounter a pre-existing dislocation loop (truncated in a dashed box in Fig. 7f). The loop also poses drag to a segment of the forward-moving dislocation line to create the large curvature, as shown in Fig. 7g. Eventually, under the effect of shear stress the long dislocation line de-trapped from the loop and atomic pinning sites, as shown in Fig. 7h. During the dislocation-loop interaction, the loop length (circumference) at first increased from 6.03 nm to 6.23 nm due to the change in local stress state. Once the dislocation line de-trapped from the loop, the loop length was reduced to 5.07 nm. The length of a dislocation loop is governed by the SFE (exerting chemical forces against climb), line tension [72,73], local Peierls friction force (or Peierls stress) [70,74] and shear stress. However, when a dislocation line driven by the shear stress glides across a loop in a concentrated solid solution such as the MEA nanopillar shown in Fig. 7e–h, the local-chemical-order can be altered, resulting in changed line tension, SFE and local Peierls friction force. As a result, the equilibrium length of the loop was reduced from 6.03 nm to 5.07 nm, as shown in Fig. 7e–h. However, the applied shear stress was insufficient to drive the loop out of the nanopillar.

Fig. 7i–l are the snapshots from Video S1, showing the von Mises atomic shear strain in the RSS, SRO, pure Ni and Cu nanopillars, respectively, corresponding to the fifth nanopillars in Fig. 4a–d. All snapshots are taken at the compressive strain of 0.08, by then stress drops have occurred a few times already. The plastic strain is carried by dislocation slip; therefore, the strain fields reveal the slip paths of dislocations. The RSS, pure Ni and Cu nanopillars show strain fields of high magnitudes in multiple slip planes and slip systems. In contrast, only a few slip planes with very strong strain fields are created in the SRO

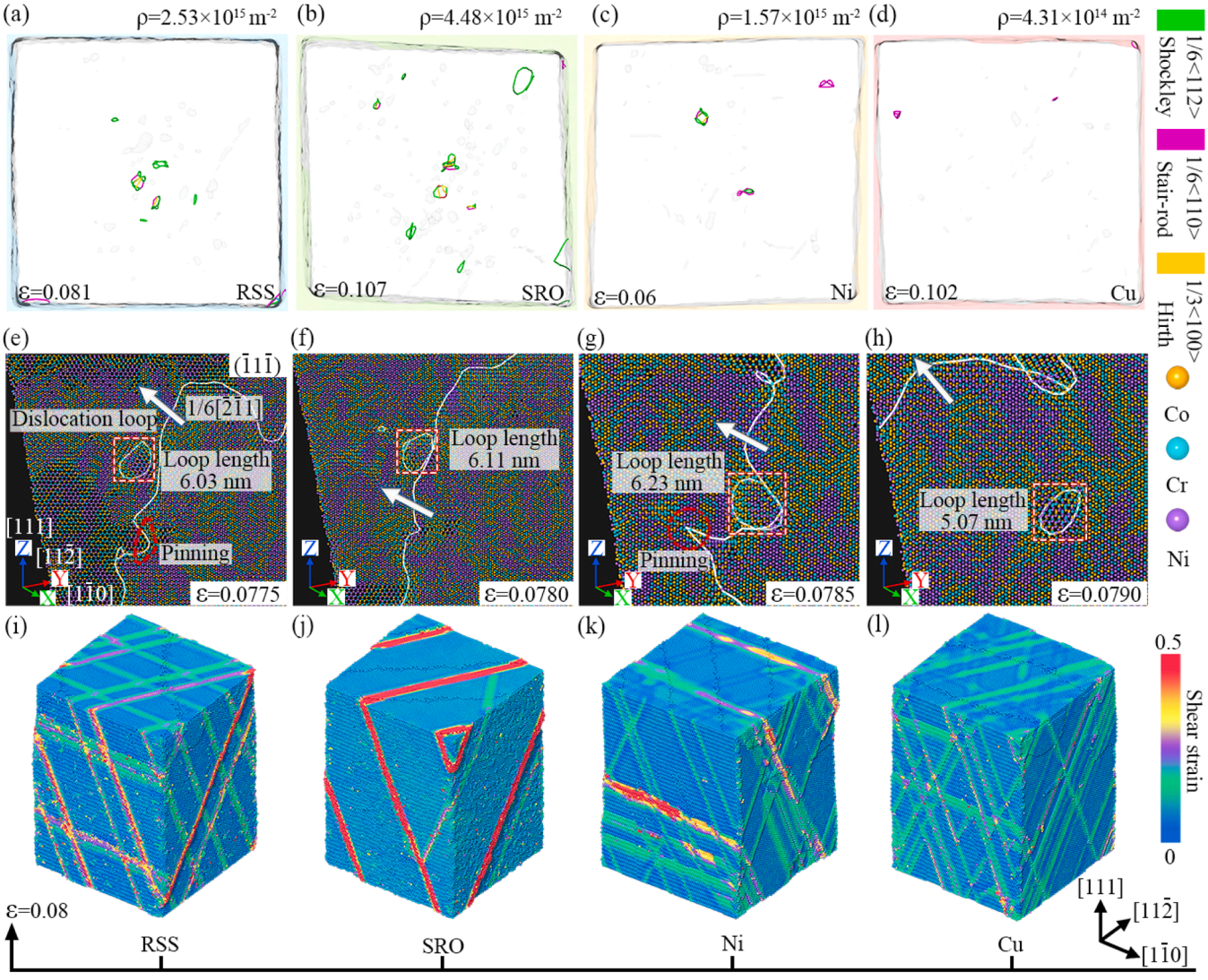

Fig. 7. Dislocations in nanopillars. (a–d) Dislocations in the RSS, SRO, pure Ni and Cu nanopillars (the fifth nanopillars in Fig. 4a–d) at the ends of stress drops, respectively. The strains are provided at the bottom left corners. (e–h) Snapshots showing a large segment of a dislocation glides across a loop in an SRO nanopillar. The white arrows indicate the slip direction of the Shockley partial dislocation. (i–l) Snapshots showing strain fields in the RSS, SRO, pure Ni and Cu nanopillars (the fifth nanopillars in Fig. 4a–d) at the compressive strain of 0.08, respectively. (The color codes for dislocations, atoms and shear strain are provided on the right-hand side column).

nanopillar, suggesting that dislocations are strictly confined to a few slip systems. This is because the local-chemical-orders, which provide high energy barriers, are broken by the leading dislocations (Fig. 5), making it much easier for subsequent dislocations to glide on the same but softened planes. Whereas many slip systems can be activated for strain accommodations in a pure metal nanopillar, because the leading dislocations pose minor effect on the energy barriers for trailing dislocations, and the choice of slip systems depends only on Schmid factors and critical resolved shear stress. The majority of the planar defects in the SRO nanopillars, formed during dislocation avalanche, are stacking faults (SFs) and multilayer hexagonal close-packed (HCP) structures, while a few nano-twins (NTs) are also observed occasionally, as shown in Supplementary information S2. NTs, SFs and multilayer HCP structures are all formed via partial dislocation emission, but the nanoscale pillar size reduces the propensity for deformation twinning [75].

3.3. The physical origin of high dislocation storage capacity

To reveal the physical origin for enhanced dislocation storage capacity and thus the resultant suppression of mechanical annealing in SRO nanopillars, local Peierls friction force F_P [70] which is the major force against the escape of dislocations is studied in detail. According to the classic Peierls model [74] for dislocation slip, the Peierls stress that drives dislocation slip is proportional to the maximum gradient along the Peierls energy profile connecting two adjacent stable dislocation positions. Utt et al. [70] proposed that analogous to the idea of Peierls stress, F_P is the maximum gradient of the local GSF energy landscape. F_P is attributed to the dislocation pinning effect by the local atom or atmosphere; therefore, it is an ideal descriptor for dislocation pinning in concentrated solid solution systems. Provided that the area per atom is not well defined in MEAs or HEAs due to strong lattice distortions, it is impractical to normalize F_P (in the unit of force, eV Å^{-1}) to stress (eV Å^{-3}). It is noteworthy that the fewer atoms used to define the local GSFE, the stronger the effect of the invariant transformation of EAM interatomic potential [76]. Therefore, the local GSFE and the corresponding gradient defined based on the potential energy of a single atom may have numerical errors. Instead of using the single value of F_P, the F_P values have to be collectively compared in order to reveal the dislocation pinning effects associated with different types of atoms.

Fig. 8a shows the global GSF energy landscape of the CoCrNi MEA. The triangular region i-ii-iii corresponds to the dissociation of a full dislocation into a pair of Shockley partials, $\frac{a}{2}[10\bar{1}] = \frac{a}{6}[11\bar{2}] + \frac{a}{6}[2\bar{1}1]$, where a is the lattice constant, and vectors i→ii and ii→iii correspond to the Burgers vectors of the leading and trailing partial dislocations, respectively [77]. The GSF energies projected on the atomic positions are symmetric, because the global GSF energy landscape has been obtained by averaging over the entire GSF plane. By conducting the steps described in Section 2.3, the local GSF energy landscape showing specific energy contribution to each atom can be obtained, as exemplified in

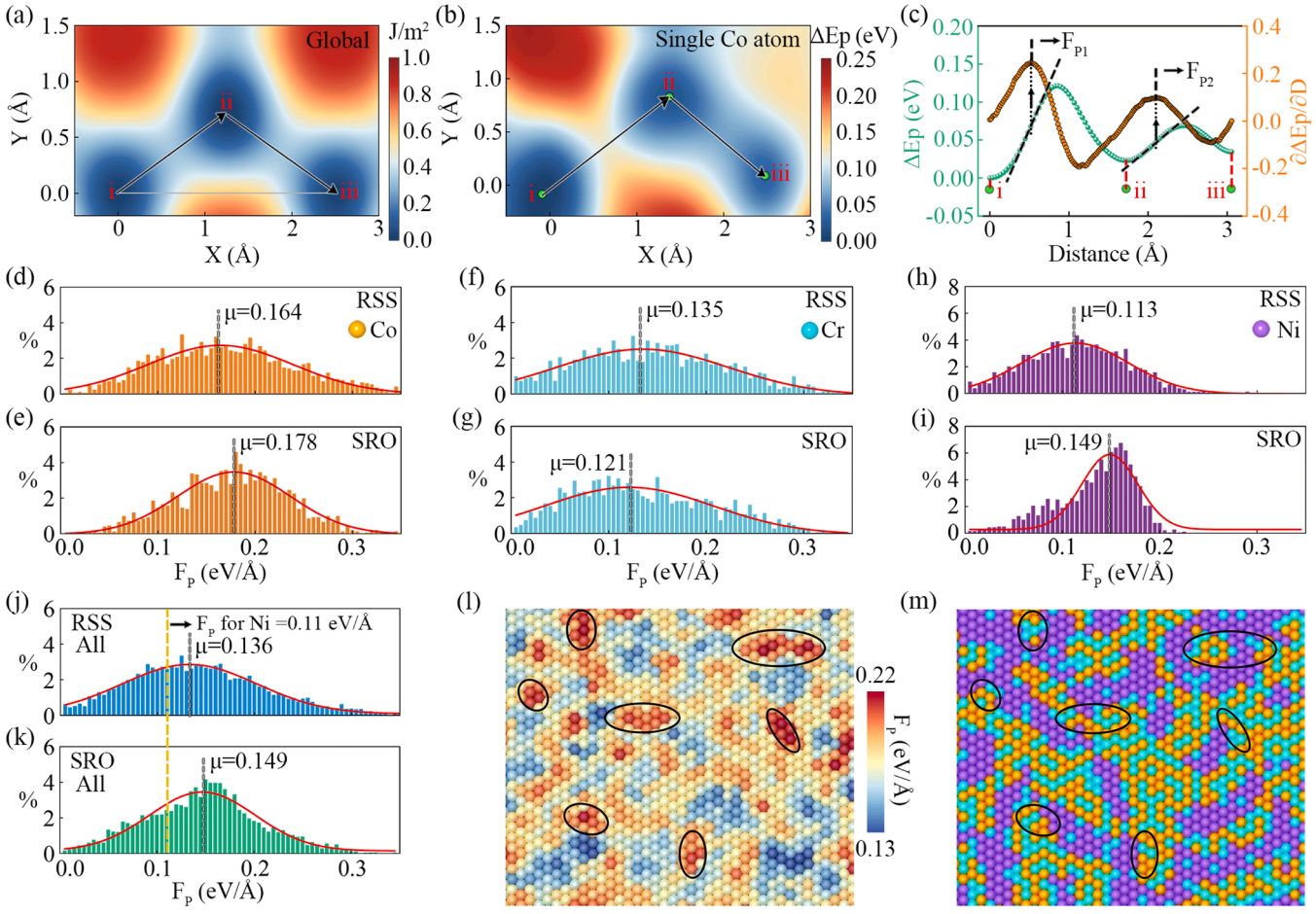

Fig. 8. GSF energy landscape and local Peierls friction force. (a) The global GSF energy landscape projected on the X-Y coordinate system for the CoCrNi MEA. (b) The local GSF energy landscape resolved for the displacement of a single atom along the path i→ii→iii. (c) The local GSF energy profile (green line) and its gradients (orange line) along the path i→ii→iii in (b). (d-i) Distributions of F_P for each type of atoms in the RSS and SRO systems. (j) and (k) show the collective distributions of F_P for all atoms. (The vertical gray dashed lines mark the means of the unimodal distribution curves, while the vertical yellow dashed line marks F_P of the pure Ni sample for the comparison purpose). (l) A map of correlated F_P (each per-atom F_P value is deduced by averaging from the surrounding atoms within the radius of 3 Å), and (m) The corresponding elemental distribution on the (111) GSF plane in the SRO CoCrNi MEA.

Fig. 8b. In this example, the local GSF energy landscape is asymmetric due to the changing chemical environment around a single Co atom during the atomic displacement [70], nonetheless three local minima marked i, ii and iii can still be identified. The local GSF energy profile associated with the displacement of the Co atom along the path i→ii→iii (Fig. 8b) is plotted as the green curve, and the gradients of the energy profile is plotted as the orange curve, as shown in Fig. 8c. Therefore, in this case, the leading partial caused the displacement of the Co atom from i to ii, and the trailing partial caused the subsequent displacement of the Co atom from ii to iii, to complete a full dislocation slip. The F_{P1} and F_{P2} marked on the two gradient peaks are thus corresponding to the local Peierls friction forces experienced by the leading and trailing partials, respectively.

We analyzed 2400 atoms on the GSF plane for each RSS and SRO model to plot the distributions of F_P for single type (Fig. 8d–i) and all atoms (Fig. 8j and k). We calculated the average value (μ) of F_P for each type of atoms, and marked the positions of μ on the bar charts with vertical gray dashed lines. As shown in Fig. 8d, e, h and i, the μ for Co and Ni in the SRO model are higher than that in the RSS model. Only the μ for Cr in the SRO model is slightly lower than that in the RSS model (Fig. 8f and g). As shown in Fig. 8j and k, $\mu = 0.149$ in the SRO model is clearly higher than $\mu = 0.136$ in the RSS model; It proves that a gliding dislocation experiences a higher pinning (force) in the SRO sample than in the RSS sample. In contrast, F_P in the pure Ni sample is a constant value 0.11 eV/Å (marked by a yellow dashed line in Fig. 8j). However, one cannot simply attribute the stronger dislocation pinning (force) in the SRO sample to Co and Ni atoms, because even for the same type of atom, its energy state may alter dramatically due to different local-chemical-order in HEAs and MEAs [18,70,78]. This is different from conventional dilute solid solutions, for which the solute atoms are surrounded by the same host atoms. Thus, we looked into a bigger picture which concerns local-chemical-order for the strong dislocation pinning effect in the SRO sample. As revealed in Fig. 8l, a map of correlated F_P is drawn by averaging F_P values from the surrounding atoms within the radius of 3 Å. Thus, the value of correlated F_P reflects implicitly the pinning point strength due to the local-chemical-order. Then the map of correlated F_P (Fig. 8l) is directly projected onto the elemental distribution map (Fig. 8m) to show the local-chemical-order structures (encircled areas in Fig. 8m) which impose strong pinning (forces) to dislocations. All of the encircled areas in Fig. 8m contain junctions of Ni cluster and Co-Cr pairs. Detailed analysis on dislocation slip in the SRO nanopillars including the example shown in Fig. 7e–h, reveals that almost all of the pre-existing dislocation loops and the strong atomic pinning sites are located at the junctions of Ni cluster and Co-Cr pairs. From the perspective of lattice strain, the large atomic size and modulus misfits between the short-range-order domain (consists of Co-Cr pairs) and the adjacent Ni cluster create a large elastic stress/strain field that poses strong resistance to dislocation slip [79]. From the perspective of free energy, the local GSF energy fluctuates strongly across the junction between the short-range-order domain having strong Co-Cr bonds [70] and the adjacent Ni cluster having strong Ni-Ni bonds [80]; As a result, the gliding dislocation tends to be trapped to the low energy valley at the junction.

As illustrated in Fig. 8m, the junctions between the short-range-order domains and the adjacent Ni clusters are closely spaced in the distance of only a few nanometers. The junction-spacing is consistent with the wavelengths of incipient concentration waves measured in HEAs [17] and the nanocrystalline NiCo solid solution alloy [79]. Therefore, we propose that the closely spaced junctions between domains and clusters impose intermittent but frequent drag to dislocation slip, thus making possible the dense pile-up and/or entanglement of dislocations inside the SRO nanopillars, as shown in Figs. 6e and 7b. It is worth noting that even in the so-called RSS (defined by the chemical short-range order parameter [55]), there are still considerable fractions of short-range-order domains and Ni clusters due to the unavoidable enthalpic interactions among the constituent elements. Therefore, the RSS nanopillars could also sustain a high dislocation density after stress drops as shown in Figs. 6e and 7a.

3.4. The sign of strain hardening

Initial dislocation densities higher than 5×10^{15} m^{-2} are introduced to all four types of nanopillars and thus expanding the data set to 55 nanopillars with initial dislocation densities in the range of 1.24×10^{15}–9.95×10^{16} m^{-2}. The reader is referred to Supplementary information S3 for details of the large data set including the stress-strain responses of the nanopillars. Fig. 9a shows that the yield stresses of the Ni and Cu nanopillars with the same dimensions of $20\times20\times30$ nm^3 decrease with increasing densities of pre-existing dislocations. This is strictly true for pure metal nanopillars of minuscule volumes in which the mean-field conditions for both forest hardening and source-truncation hardening break down [9,11,81], and thus exhaustion hardening is in sole dominance. However, the yield stresses of the RSS and SRO MEA nanopillars tend to level off when the initial dislocation densities are larger than $\sim2.00\times10^{16}$ m^{-2}, suggesting that exhaustion hardening ceases to operate at such high dislocation densities. Nevertheless, moderate scattering of data points with respect to the linear decreasing trend, can be seen in Fig. 9a. This is because that the correlation between the yield stress and initial dislocation density is affected by many factors such as the types of dislocations, number of dislocation multi-junctions, distances of dislocations to the pillar surface. For example, stair-rod and Hirth dislocations can help to sustain a high yield stress, but free-standing Shockley partials (exist in majority) reduce the yield stress. However, the influences of these factors on yield stresses are limited for nanopillars, because a large number of dislocations tend to quickly escape from the confined volume.

Figs. 9b and c show the stress-strain curves and corresponding dislocation density evolutions for the nanopillars marked by black arrows in Fig. 9a. The Ni and Cu nanopillars yielded at very low stresses but gradually gained stresses with intermittent stress drops; After yielding, the dislocation densities in the Ni and Cu nanopillars continuously decreased with minor undulations. Apparently, mechanical annealing is active in the Ni and Cu nanopillars with high initial dislocation densities, and the resultant increasing stress with decreasing dislocation density demonstrates the exhaustion hardening. In contrast, the SRO nanopillar yielded at a high stress of 4.72 GPa and strengthened further to 5.79 GPa at the strain of 0.0345. Correspondingly, the dislocation density in the SRO nanopillar (Fig. 9c) actually increased with the increasing stress (Fig. 9b) within the greenish column, thus demonstrating the phenomenon that resembles forest hardening. Fig. 9d and e show the dislocation activities that contribute to the strain hardening in the strain range of 0.03–0.0345. As shown in Fig. 9d, at $\varepsilon = 0.03 - 0.315$, dislocation nets marked 1 and 2 stay stationary while the Shockley partial dislocation 3 glides towards the nets 1 and 2 on the slip plane ACD. At $\varepsilon = 0.032$, the Shockley partial dislocation 3 encounters the nets 1 and 2, and is pinned to stop. Consequently, dislocation 3 and nets 1 and 2 are mutually trapped to form a large metastable dislocation net 3'-2-3''-1-3'', as shown in Fig. 9d. Once the dislocation interactions come to a stop (Fig. 9d), the Lomer-Cottrell lock shown in Fig. 9e begins to unravel at $\varepsilon = 0.0325$; The Shockley partial dislocations on planes ABD and ACD become mobile and glide away from the original locked position marked by the black dashed-lines. At $\varepsilon = 0.0345$, the Shockley partial dislocations are tangled again to form new stair-rod and Hirth dislocations. Meanwhile, in the strain range $\varepsilon = 0.03$–0.345, activation of surface source was undetected, the increase in dislocation density has been attributed to extension of dislocation lines and interactions between dislocations, as shown in Fig. 9d and e. Hence, instead of exhaustion hardening, strain hardening due mutual trapping and accumulation of dislocations occurred in the SRO nanopillar. By the way, dislocation entanglement also occurred in the RSS nanopillar, but the dislocation density gradually decreases with increasing strain as shown in Fig. 9c, indicating that mechanical annealing is still moderately active

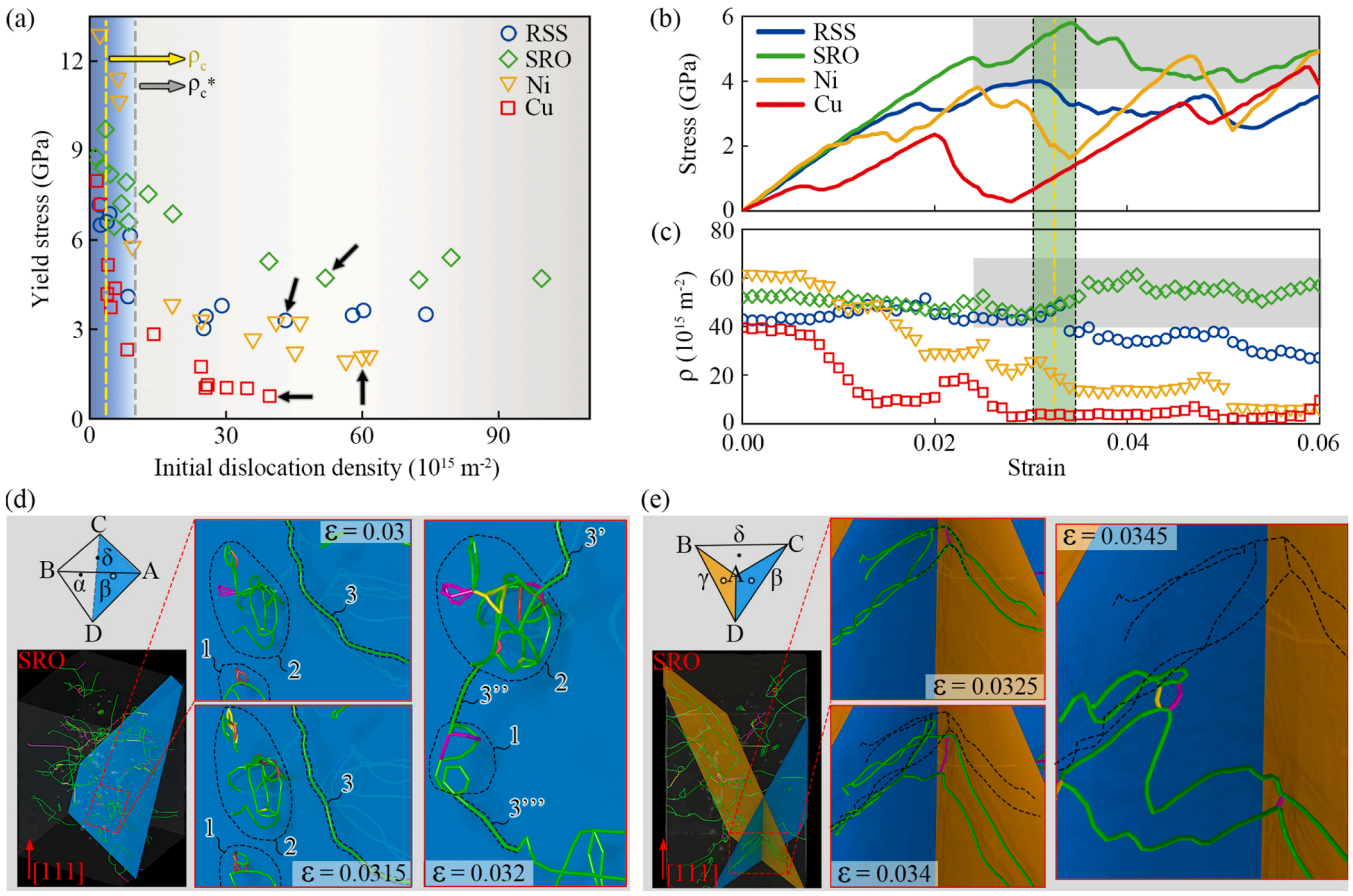

Fig. 9. The relationship between initial dislocation density and flow stress. (a) Yield stress versus initial dislocation density. (b) and (c) show the stress-strain curves and evolution of dislocation density for nanopillars with high densities of pre-existing dislocations; The corresponding samples are marked by black arrows in (a). (d) Interactions between a Shockley partial dislocation and pre-entangled dislocations as the shear strain increased from $\varepsilon = 0.03 \sim 0.032$. (e) Mobilization of interlocked dislocations at the shear strain of $\varepsilon = 0.0325 \sim 0.0345$. The Thompson tetrahedron is provided to help illustrate active slip planes. The same color code for dislocations in Fig. 7 is used in this figure.

and counteracting against strain hardening in the RSS nanopillar. Evolution of dislocations in nanopillars with pre-saturated dislocation networks is shown in Video S2.

4. Discussion

In this section, the commonly seen mechanical annealing phenomenon in pure metal nanopillars is revisited. In contrast to pure metal nanopillars, suppression of mechanical annealing in the CoCrNi single-crystalline nanopillars is justified and discussed. Furthermore, the underlying physics for the transition from exhaustion hardening to strain hardening in the SRO CoCrNi nanopillars is verified and discussed.

4.1. Mechanical annealing in pure metals

The strength and plasticity of the single crystals with sizes below submicrometer are different from those of the bulk samples. For the most studied FCC nanopillars, such as Ni, Cu and Al nanopillars, they show extremely high mechanical strength and fluctuations of stress-strain curves [1,68,82]. The apparent fluctuation of flow stress is attributed to repeated dislocation exhaustion (mechanical annealing) and dislocation avalanche in the single crystals of extremely small dimensions [2,16,83,84]. The Cu and Ni nanopillars simulated in this work exhibit the characteristics of plastic deformation, such as intermittent stress rises/drops (Fig. 4c and d) and continuous rise and fall of dislocation densities (Fig. 6a–d). Provided that dislocations are the major plastic strain carriers in nanopillars, a sufficient number of mobile dislocations is required to accommodate the plastic strain. The mobile dislocations can be the pre-existing dislocations and/or be generated by dislocation sources. In nanopillars with the diameters or diagonal lengths of only a few tens of nanometers, the densities of pre-existing dislocations are usually in the range $\sim 10^{12} - 10^{15}$ m^{-2} [65], corresponding to only a few short dislocations which are far from sufficient for strain accommodation [11]. Meanwhile, the Frank-Read source and single-arm source cease to operate due to insufficient activation volumes in nanopillars [11,85]. Therefore, under compressive deformation the stress increases linearly while the majority of the pre-existing dislocations lay dormant in low energy states until a sufficient high stress is reached to simultaneously activate surface sources [10] and pre-existing dislocations; This is corresponding to the near elastic loading segment attained at initial loading, as shown in Fig. 4a–d. Once the first peak stress is reached, dislocation avalanche suddenly occurs to accommodate the plastic strain. Meanwhile, under the strong effects of shear stress, image force [8,86] and repulsive force [14] between dislocations, the mobile dislocations quickly escape from the nanopillar surface, resulting in the observed mechanical annealing as shown in Fig. 6 and the Video S1.

4.2. Suppression of mechanical annealing

Detailed analysis on the dislocation density evolutions from statistical data and videos, reveals that the extent of mechanical annealing for MEA nanopillars differ significantly from the pure metal nanopillars. As shown in Fig. 6, the dislocation densities of the MEA nanopillars could be retained above 2.45×10^{15} m^{-2}, in contrast the dislocation densities

could even reach zero for pure metal nanopillars for complete mechanical annealing. As discussed in previous section, gliding dislocations in MEA nanopillars experience very strong local Peierls friction force when traversing junctions between the short-range-order domains and the adjacent Ni clusters. The strong local Peierls friction forces not only slow down dislocation slip, but also increase the probability for dislocation entanglement; as a result, significant numbers of dislocations could be retained after dislocation avalanche in the MEA nanopillars. In contrast, in pure metal nanopillars gliding dislocations experience only nearly constant lattice friction forces which can be partially or even completely balanced out by strong image forces, hence most of the mobile dislocations require low shear stress to escape from the nanopillar surface; correspondingly, the stress could drop to a few megapascals as shown in Fig. 4c and d.

As described by Hooke's law, $\sigma = E\varepsilon$, the elastic stress σ is linearly proportional to the elastic strain ε. Provided that the Young's modulus E stays a constant for the same material at a constant temperature, the increased elastic strain with increasing elastic stress manifests the prolonged elastic loading segment. Nanopillars experience exhaustion hardening that the stress increases with decreasing dislocation density [2,9], and thus manifests prolonged nearly elastic loading and reloading segments, as shown in Fig. 4a–d. As shown in Fig. 4c and d and Fig. 6a–d, in despite of the different initial dislocation densities, the stresses would drop below 1 GPa for all Ni and Cu nanopillars after first one or two stress drops, and correspondingly the dislocation densities decreased below $\sim 2\times10^{15}$ m^{-2} as a result of mechanical annealing; The low dislocation densities provide room for again prolonged reloading segments, as shown in Fig. 4e and f. On the other hand, mechanical annealing was suppressed in the MEA nanopillars, the stresses were kept above 2 GPa after stress drops, and the dislocation densities sustained at comparatively high levels above 2.45×10^{15} m^{-2}, as shown in Figs. 4a, b and 6. The high densities of retained dislocations reduced the effect of exhaustion hardening; Therefore, reloading segments are short and the reloading strains are low for the MEA nanopillars (Fig. 4a, b, e and f). The compressive stress-strain curves of the Ni pillars [2] and the CrCoNi pillars [87] obtained by *in-situ* experiments, show that the relative load drop after strain burst is lower for the CrCoNi pillars. Therefore, the experimental results [87–89] are supportive to our simulation results of suppressed mechanical annealing in MEA/HEA nanopillars. Dislocation activities in HEA nanopillars have also been studied previously. For example, dislocation pile-ups after dislocation avalanche are observed in the FCC $Al_{0.1}$CoCrFeNi HEA nanopillars, indicating that the dislocation networks are not completely exhausted during the stress drop [90]. In a body-centered cubic (BCC) HEA nanopillar with a diameter of only ~300 nm, pronounced dislocation interactions, entanglement and accumulations were observed during compressive deformation, resulting in apparent strain hardening [91].

4.3. Transition from exhaustion hardening to strain hardening

As shown in Fig. 6e, the SRO nanopillars show increased dislocation densities after stress drops, giving the sign of dislocation accumulation in MEA nanopillars. This distinct result makes us wonder to what extent can dislocations accumulate while the mechanical annealing is apparently suppressed in MEA pillars? In other words, what is the consequence of suppressed mechanical annealing for the plastic deformation of MEA nanopillars?

There has been a transition from exhaustion hardening to some sort of strain hardening in the SRO nanopillars with increasing dislocation density, as shown in Fig. 9. Similar phenomenon has been observed in larger nanopillars [9,11], and has been confirmed to be the transition from exhaustion hardening to source-truncation hardening [6,92]. Based on the in-depth survey of literatures [2,9,11,12], we propose that the underlaying physics of exhaustion hardening in nanopillars coincide with the strain-rate hardening mechanism in defect-scarce crystals [12] that can be explained as follows: knowing that dislocations cannot glide faster than a maximum velocity (v_{max}) due to strong electron and phonon drags [93,94], when all the mobile dislocations gliding at v_{max} cannot keep up with the strain rate, extremely high stresses close to the theoretical strength of the material are needed to activate surface sources [10,7,95]. Therefore, there shall be a critical dislocation density for exhaustion hardening [2,9,12], above which there may be the transition to strain hardening. Under the assumptions that all mobile dislocations are gliding at v_{max} and mutual trapping of dislocations is negligible, the critical dislocation density for exhaustion hardening can be estimated as (the detail of formulation is provided in Supplementary information S4) [12]:

$$\rho_c = \left(\frac{2\dot{\varepsilon}\left(\frac{\eta Gb}{v_{max}}\right)}{\alpha m f_a G b^3} \right)^{\frac{2}{3}} \tag{1}$$

where G is the shear modulus provided in Table 1, b is the Burgers vector which can be deduced based on the lattice constant provided in Table 1, $\dot{\varepsilon} = 10^8\ s^{-1}$ is the strain rate used in this work, $f_a = 2/3$ is the fraction of mobile dislocations (a simplified estimation [12]), $\alpha = 0.1$ is a dimensionless constant [96], $\eta \approx 0.002$ is the viscosity [12,93] and v_{max} is obtained from MD simulations (Supplementary information S4). By using Eq. (1), the $\rho_c = 3.5314\times10^{15}$ m^{-2} is found for the SRO nanopillar and marked by the yellow dashed-line in Fig. 9a. However, according to our simulation results, strain hardening (substantial dislocation entanglement) becomes noticeable at $\rho_c^* = \sim1\times10^{16}$ m^{-2}, marked by the gray dashed-line in Fig. 9a. The measured critical dislocation density for exhaustion hardening ρ_c^* is higher than the theoretical ρ_c. This is because Eq. (1) does not account for the strong local Peierls friction forces and mutual trapping of dislocations that can substantially reduce the dislocation velocity. Therefore, in practice a nanopillar can have a dislocation density higher than the theoretical ρ_c, but still demonstrate exhaustion hardening. However, a dislocation density higher than ρ_c or ρ_c^* does not guarantee the transition to strain hardening. As shown in Fig. 9b and c, for the Ni and Cu nanopillars with initial dislocation densities higher than $\sim1\times10^{16}$ m^{-2}, the dislocation densities decrease with increasing strain via the mechanical annealing mechanism to eventually show exhaustion hardening again. Therefore, it is concluded that suppression on mechanical annealing and the transition from exhaustion hardening to strain hardening in nanopillars are both affected by the pillar size, strain rate, and in the current case short range ordering.

5. Conclusions

In summary, the continuous elastic to plastic deformation of MEA CoCrNi nanopillars with different chemical ordering and initial dislocation densities have been investigated in detail. Pure metal Ni and Cu nanopillars of the same size and with similar initial dislocation densities are used as reference samples.

By quantitatively analyzing dislocation activities and local Peierls friction forces, we reveal the origin of large dislocation storage capacities in CoCrNi MEA single-crystalline nanopillars. The MEA nanopillars containing SRO domains demonstrate strong local Peierls friction forces that can pose strong resistance to dislocation slip and hence to increase the probability of dislocation entanglement and the capacity of dislocation storage. Consequently, the MEA nanopillars show suppressed mechanical annealing in contrast to pure metal nanopillars with obvious mechanical annealing.

Although pure Ni and Cu can accommodate large dislocation densities ($\sim5\times10^{16}$ m^{-2}) at some point of the elastoplastic transition, eventually dislocations tend to be exhausted at the onset of plastic deformation. Therefore, exhaustion hardening is verified the only collective dislocation mechanism for pure Ni and Cu nanopillars, despite of different pre-existing dislocation densities.

While mechanical annealing is reluctant in MEA nanopillars, with the increase of dislocation density above $\rho_c^* = \sim 1\times10^{16}$ m^{-2}, the transition from exhaustion hardening to strain hardening occurred in the MEA nanopillars, especially the SRO MEA nanopillars. The transition of hardening mechanisms is mainly determined by the composition complexity and SRO. The strong lattice friction can balance out the image force, and thus sustaining stable dislocation networks and enabling large storage of dislocations. This has been the first ever simulation result to show substantial dislocation accumulation and thus strain hardening in nanopillars with such small diagonal lengths or diameters.

CRediT authorship contribution statement

Luling Wang: Writing – original draft, Visualization, Software, Methodology, Formal analysis. **Chi Xu:** Writing – original draft, Software, Methodology, Data curation. **Binpeng Zhu:** Investigation, Data curation. **Jizi Liu:** Investigation, Data curation. **Ningning Liang:** Investigation, Data curation. **Runchang Liu:** Investigation, Data curation. **Yang Cao:** Writing – review & editing, Supervision, Resources, Investigation, Funding acquisition. **Yonghao Zhao:** Writing – review & editing, Supervision, Resources, Funding acquisition.

Declaration of competing interest

The authors declare that they have no known competing financial interests or personal relationships that could have appeared to influence the work reported in this paper.

Acknowledgments

This work is funded by the National Key R&D Program of China (Grant No. 2021YFA1200203), the National Natural Science Foundation of China (Grant Nos. 51971112, 51225102 and 52071181), the Six Talent Peaks Project of Jiangsu Province (Grant No. 2017-XCL-051), and Jiangsu Province Leading Edge Technology Basic Research Major Project (BK20222014). The authors are grateful to Dr. Daniel Utt and Dr. Alexander Stukowski for the helpful discussions regarding the simulation work of local Peierls friction forces.

Supplementary materials

Supplementary material associated with this article can be found, in the online version, at doi:10.1016/j.ijmecsci.2025.109979.

Data availability

Data will be made available on request.

References

[1] Uchic MD, Dimiduk DM, Florando JN, Nix WD. Sample dimensions influence strength and crystal plasticity. Science 2004;305:986–9.
[2] Shan ZW, Mishra RK, Syed Asif SA, Warren OL, Minor AM. Mechanical annealing and source-limited deformation in submicrometre-diameter Ni crystals. Nat Mater 2008;7:115–9.
[3] Shulaker MM, Hills G, Park RS, Howe RT, Saraswat K, Wong HSP, et al. Three-dimensional integration of nanotechnologies for computing and data storage on a single chip. Nature 2017;547:74–8.
[4] Bayda S, Adeel M, Tuccinardi T, Cordani M, Rizzolio F. The history of nanoscience and nanotechnology: from chemical–physical applications to nanomedicine. Molecules 2019;25:112.
[5] Spearing SM. Materials issues in microelectromechanical systems (MEMS). Acta Mater 2000;48:179–96.
[6] Tang H, Schwarz KW, Espinosa HD. Dislocation-source shutdown and the plastic behavior of single-crystal micropillars. Phys Rev Lett 2008;100:185503.
[7] Chen LY, He M, Shin J, Richter G, Gianola DS. Measuring surface dislocation nucleation in defect-scarce nanostructures. Nat Mater 2015;14:707–13.
[8] Li QJ, Xu B, Hara S, Li J, Ma E. Sample-size-dependent surface dislocation nucleation in nanoscale crystals. Acta Mater 2018;145:19–29.
[9] Rao SI, Dimiduk DM, Parthasarathy TA, Uchic MD, Tang M, Woodward C. Athermal mechanisms of size-dependent crystal flow gleaned from three-dimensional discrete dislocation simulations. Acta Mater 2008;56:3245–59.
[10] Zhu T, Li J, Samanta A, Leach A, Gall K. Temperature and strain-rate dependence of surface dislocation nucleation. Phys Rev Lett 2008;100:025502.
[11] Jennings AT, Li J, Greer JR. Emergence of strain-rate sensitivity in Cu nanopillars: Transition from dislocation multiplication to dislocation nucleation. Acta Mater 2011;59:5627–37.
[12] Fan H, Wang Q, El-Awady JA, Raabe D, Zaiser M. Strain rate dependency of dislocation plasticity. Nat Commun 2021;12:1845.
[13] Brochard S, Hirel P, Pizzagalli L, Godet J. Elastic limit for surface step dislocation nucleation in face-centered cubic metals: Temperature and step height dependence. Acta Mater 2010;58:4182–90.
[14] Srivastava K, Weygand D, Caillard D, Gumbsch P. Repulsion leads to coupled dislocation motion and extended work hardening in bcc metals. Nat Commun 2020;11:5098.
[15] Oh SH, Legros M, Kiener D, Dehm G. *In situ* observation of dislocation nucleation and escape in a submicrometre aluminium single crystal. Nat Mater 2009;8:95–100.
[16] Greer JR, Nix WD. Nanoscale gold pillars strengthened through dislocation starvation. Phys Rev B 2006;73:245410.
[17] Ding Q, Zhang Y, Chen X, Fu X, Chen D, Chen S, et al. Tuning element distribution, structure and properties by composition in high-entropy alloys. Nature 2019;574:223–7.
[18] Li QJ, Sheng H, Ma E. Strengthening in multi-principal element alloys with local-chemical-order roughened dislocation pathways. Nat Commun 2019;10:3563.
[19] Gludovatz B, Hohenwarter A, Thurston KVS, Bei H, Wu Z, George EP, et al. Exceptional damage-tolerance of a medium-entropy alloy CrCoNi at cryogenic temperatures. Nat Commun 2016;7:10602.
[20] Ma E, Liu C. Chemical inhomogeneities in high-entropy alloys help mitigate the strength-ductility trade-off. Prog Mater Sci 2024;143:101252.
[21] Wang L, Ding J, Chen S, Jin K, Zhang Q, Cui J, et al. Tailoring planar slip to achieve pure metal-like ductility in body-centred-cubic multi-principal element alloys. Nat Mater 2023;22:950–7.
[22] Wu Y, Zhang F, Yuan X, Huang H, Wen X, Wang Y, et al. Short-range ordering and its effects on mechanical properties of high-entropy alloys. J Mater Sci Technol 2021;62:214–20.
[23] Zhang M, Yu Q, Frey C, Walsh F, Payne MI, Kumar P, et al. Determination of peak ordering in the CrCoNi medium-entropy alloy via nanoindentation. Acta Mater 2022;241:118380.
[24] Li L, Chen Z, Kuroiwa S, Ito M, Yuge K, Kishida K, et al. Evolution of short-range order and its effects on the plastic deformation behavior of single crystals of the equiatomic Cr-Co-Ni medium-entropy alloy. Acta Mater 2023;243:118537.
[25] Chen S, Aitken ZH, Pattamatta S, Wu Z, Yu ZG, Srolovitz DJ, et al. Crack tip dislocation activity in refractory high-entropy alloys. Int J Mech Sci 2024;262:108753.
[26] Koželj P, Vrtnik S, Jelen A, Jazbec S, Jagličić Z, Maiti S, et al. Discovery of a superconducting high-entropy alloy. Phys Rev Lett 2014;113:107001.
[27] Pasianot R, Farkas D. Atomistic modeling of dislocations in a random quinary high-entropy alloy. Comput Mater Sci 2020;173:109366.
[28] Ruestes CJ, Farkas D. Dislocation emission and propagation under a nano-indenter in a model high entropy alloy. Comput Mater Sci 2022;205:111218.
[29] Wang L, Cao Y, Zhao Y. Lattice distortion promotes incipient plasticity in multiprincipal element alloys. Nano Lett 2024;24:9004–10.
[30] He T, Qi Y, Ji Y, Feng M. Grain boundary segregation-induced strengthening-weakening transition and its ideal maximum strength in nanopolycrystalline FeNiCrCoCu high-entropy alloys. Int J Mech Sci 2023;238:107828.
[31] Farkas D, Caro A. Model interatomic potentials for Fe–Ni–Cr–Co–Al high-entropy alloys. J Mater Res 2020;35:3031–40.
[32] Yin S, Zuo Y, Abu-Odeh A, Zheng H, Li XG, Ding J, et al. Atomistic simulations of dislocation mobility in refractory high-entropy alloys and the effect of chemical short-range order. Nat Commun 2021;12:4873.
[33] Zhang FX, Zhao S, Jin K, Xue H, Velisa G, Bei H, et al. Local structure and short-range order in a NiCoCr solid solution alloy. Phys Rev Lett 2017;118:205501.
[34] Zhang R, Zhao S, Ding J, Chong Y, Jia T, Ophus C, et al. Short-range order and its impact on the CrCoNi medium-entropy alloy. Nature 2020;581:283–7.
[35] An Z, Li A, Mao S, Yang T, Zhu L, Wang R, et al. Negative mixing enthalpy solid solutions deliver high strength and ductility. Nature 2024:697–702.
[36] Jian WR, Xie Z, Xu S, Su Y, Yao X, Beyerlein IJ. Effects of lattice distortion and chemical short-range order on the mechanisms of deformation in medium entropy alloy CoCrNi. Acta Mater 2020;199:352–69.
[37] Lu W. A hierarchical multiscale crystal plasticity model for refractory multi-principal element alloys. Int J Mech Sci 2024;271:109140.
[38] Ma S, Liu W, Li Q, Zhang J, Huang S, Xiong Y, et al. Mechanism of elemental segregation around extended defects in high-entropy alloys and its effect on mechanical properties. Acta Mater 2024;264:119537.
[39] Wang Z, Wu H, Wu Y, Huang H, Zhu X, Zhang Y, et al. Solving oxygen embrittlement of refractory high-entropy alloy via grain boundary engineering. Mater Today 2022;54:83–9.
[40] Bian B, Söltzer L, Muralikrishna GM, Taheriniya S, Sen S, Hari Kumar KC, et al. Grain boundary diffusion in a compositionally complex alloy: Interplay of segregation, precipitation and interface structures in a Ni–Cr–Mo alloy. Acta Mater 2024;269:119803.
[41] Li XT, Tang XZ, Guo YF, Li H, Fan Y. Modulating grain boundary-mediated plasticity of high-entropy alloys via chemo-mechanical coupling. Acta Mater 2023;258:119228.

[42] Zhu J, Sun L, Li D, Zhu L, He X. Compositional undulation induced strain hardening and delocalization in multi-principal element alloys. Int J Mech Sci 2023;241:107931.
[43] Sohn SS, Kwiatkowski da Silva A, Ikeda Y, Körmann F, Lu W, Choi WS, et al. Ultrastrong medium-entropy single-phase alloys designed via severe lattice distortion. Adv Mater 2019;31:1807142.
[44] Han Z, Ma Z, Shen G, Zhang W, Li J, Li Y, et al. An additively manufactured high-entropy alloy with superior wear resistance by nanoprecipitation and high density dislocations. Tribol Int 2024;199:109993.
[45] Li H, Han Y, Feng H, Zhou G, Jiang Z, Cai M, et al. Enhanced strength-ductility synergy via high dislocation density-induced strain hardening in nitrogen interstitial CrMnFeCoNi high-entropy alloy. J Mater Sci Technol 2023;141:184–92.
[46] Gu L, Zhao Y, Li Y, Hou R, Liang F, Zhang R, et al. Ultrastrong and ductile medium-entropy alloys via hierarchical ordering. Sci Adv 2024;10:eadn7553.
[47] Jiang W, Yuan S, Cao Y, Zhang Y, Zhao Y. Mechanical properties and deformation mechanisms of a $Ni_2Co_1Fe_1V_{0.5}Mo_{0.2}$ medium-entropy alloy at elevated temperatures. Acta Mater 2021;213:116982.
[48] Plimpton S. Fast parallel algorithms for short-range molecular dynamics. J Comput Phys 1995;117:1–19.
[49] Ding J, Yu Q, Asta M, Ritchie RO. Tunable stacking fault energies by tailoring local chemical order in CrCoNi medium-entropy alloys. Proc Natl Acad Sci 2018;115:8919–24.
[50] Mishin Y, Mehl MJ, Papaconstantopoulos DA, Voter AF, Kress JD. Structural stability and lattice defects in copper: ab initio, tight-binding, and embedded-atom calculations. Phys Rev B 2001;63:224106.
[51] Hirel P. Atomsk: A tool for manipulating and converting atomic data files. Comput Phys Commun 2015;197:212–9.
[52] Sadigh B, Erhart P, Stukowski A, Caro A, Martinez E, Zepeda-Ruiz L. Scalable parallel Monte Carlo algorithm for atomistic simulations of precipitation in alloys. Phys Rev B 2012;85:184203.
[53] Sadigh B, Erhart P. Calculation of excess free energies of precipitates via direct thermodynamic integration across phase boundaries. Phys Rev B 2012;86:134204.
[54] Dullweber A, Leimkuhler B, McLachlan R. Symplectic splitting methods for rigid body molecular dynamics. J Chem Phys 1997;107:5840–51.
[55] De Fontaine D. The number of independent pair-correlation functions in multicomponent systems. J Appl Crystallogr 1971;4:15–9.
[56] Lee S, Jeong J, Kim Y, Han SM, Kiener D, Oh SH. FIB-induced dislocations in Al submicron pillars: Annihilation by thermal annealing and effects on deformation behavior. Acta Mater 2016;110:283–94.
[57] Ruestes CJ, Farkas D. Deformation response of high entropy alloy nanowires. J Mater Sci 2021;56:16447–62.
[58] Norman JE, Wang X, Dupuy AD, Schoenung JM. Micropillar compression of single-crystal single-phase (Co, Cu, Mg, Ni, Zn)O. Applied Physics Letters 2024;125:031901.
[59] Stukowski A. Visualization and analysis of atomistic simulation data with OVITO–the open visualization tool. Model Simul Mater Sci Eng 2010;18:015012.
[60] Stukowski A, Bulatov VV, Arsenlis A. Automated identification and indexing of dislocations in crystal interfaces. Modelling Simul Mater Sci Eng 2012;20:085007.
[61] Stukowski A, Albe K. Extracting dislocations and non-dislocation crystal defects from atomistic simulation data. Modelling Simul Mater Sci Eng 2010;18:085001.
[62] Shimizu F, Ogata S, Li J. Theory of shear banding in metallic glasses and molecular dynamics calculations. Mater Trans 2007;48:2923–7.
[63] Guénolé J, Nöhring WG, Vaid A, Houllé F, Xie Z, Prakash A, et al. Assessment and optimization of the fast inertial relaxation engine (fire) for energy minimization in atomistic simulations and its implementation in lammps. Comput Mater Sci 2020;175:109584.
[64] Virtanen P, Gommers R, Oliphant TE, Haberland M, Reddy T, Cournapeau D, et al. SciPy 1.0: fundamental algorithms for scientific computing in Python. Nat Methods 2020;17:261–72.
[65] Fu L, Yang C, Wei R, Pei X, Teng J, Kong D, et al. *In situ* atomic-scale observation of AuCu alloy nanowire with superplasticity and high strength at room temperature. Mater Today Nano 2021;15:100123.
[66] Giwa AM, Aitken ZH, Liaw PK, Zhang YW, Greer JR. Effect of temperature on small-scale deformation of individual face-centered-cubic and body-centered-cubic phases of an $Al_{0.7}$CoCrFeNi high-entropy alloy. Mater Des 2020;191:108611.
[67] Imrich PJ, Kirchlechner C, Kiener D, Dehm G. Internal and external stresses: *in situ* TEM compression of Cu bicrystals containing a twin boundary. Scr Mater 2015;100:94–7.
[68] Jennings AT, Burek MJ, Greer JR. Microstructure versus size: mechanical properties of electroplated single crystalline Cu nanopillars. Phys Rev Lett 2010;104:135503.
[69] Nix WD, Greer JR, Feng G, Lilleodden ET. Deformation at the nanometer and micrometer length scales: Effects of strain gradients and dislocation starvation. Thin Solid Films 2007;515:3152–7.
[70] Utt D, Lee S, Xing Y, Jeong H, Stukowski A, Oh SH, et al. The origin of jerky dislocation motion in high-entropy alloys. Nat Commun 2022;13:4777.
[71] Farkas D. The role of compositional complexity in the increased fracture resistance of high entropy alloys: Multi-scale atomistic simulations. Comput Mater Sci 2024;235:112758.
[72] Schmid H, Kirchner HOK. Self-stress and equilibrium shapes of dislocation loops. Philos Mag A 1988;58:905–21.
[73] Lee FFM, Shyne JC, Nix WD. Self stresses and line tensions in dislocation loops. Mater Sci Eng 1968;3:175–82.
[74] Nabarro FRN. Fifty-year study of the Peierls-Nabarro stress. Mater Sci Eng A 1997;234–236:67–76.
[75] Wu XL, Zhu YT. Inverse grain-size effect on twinning in nanocrystalline Ni. Phys Rev Lett 2008;101:025503.
[76] Daw MS, Foiles SM, Baskes MI. The embedded-atom method: a review of theory and applications. Mater Sci Rep 1993;9:251–310.
[77] Pei Z, Zhang S, Lei Y, Zhang F, Chen M. Decoupling between Shockley partials and stacking faults strengthens multiprincipal element alloys. Proc Natl Acad Sci U S A 2021;118:e2114167118.
[78] Naghdi AH, Karimi K, Poisvert AE, Esfandiarpour A, Alvarez R, Sobkowicz P, et al. Dislocation plasticity in equiatomic NiCoCr alloys: Effect of short-range order. Phys Rev B 2023;107:094109.
[79] Li H, Zong H, Li S, Jin S, Chen Y, Cabral MJ, et al. Uniting tensile ductility with ultrahigh strength via composition undulation. Nature 2022;604:273–9.
[80] Xing B, Wang X, Bowman WJ, Cao P. Short-range order localizing diffusion in multi-principal element alloys. Scr Mater 2022;210:114450.
[81] Wang P, Liu F, Cui Y, Liu Z, Qu S, Zhuang Z. Interpreting strain burst in micropillar compression through instability of loading system. Int J Plast 2018;107:150–63.
[82] Kunz A, Pathak S, Greer JR. Size effects in Al nanopillars: Single crystalline vs. bicrystalline. Acta Mater 2011;59:4416–24.
[83] Griesbach C, Jeon SJ, Rojas DF, Ponga M, Yazdi S, Pathak S, et al. Origins of size effects in initially dislocation-free single-crystal silver micro and nanocubes. Acta Mater 2021;214:117020.
[84] Lee SW, Nix WD. Size dependence of the yield strength of fcc and bcc metallic micropillars with diameters of a few micrometers. Philos Mag 2012;92:1238–60.
[85] Nix WD, Lee S-W. Micro-pillar plasticity controlled by dislocation nucleation at surfaces. Philos Mag 2011;91:1084–96.
[86] Cui YN, Lin P, Liu ZL, Zhuang Z. Theoretical and numerical investigations of single arm dislocation source controlled plastic flow in FCC micropillars. Int J Plast 2014;55:279–92.
[87] Zhang Z, Sheng H, Wang Z, Gludovatz B, Zhang Z, George EP, et al. Dislocation mechanisms and 3D twin architectures generate exceptional strength-ductility-toughness combination in CrCoNi medium-entropy alloy. Nat Commun 2017;8:14390.
[88] Zhang Q, Niu R, Liu Y, Jiang J, Xu F, Zhang X, et al. Room-temperature super-elongation in high-entropy alloy nanopillars. Nat Commun 2023;14:7469.
[89] Liu NJ, Wang ZJ, Ding J, Asta M, Ritchie RO, Gan B, et al. Origin of the high propensity for nanoscale deformation twins in CrCoNi medium-entropy alloy. J Mater Sci Technol 2024;183:63–71.
[90] Hu Y, Shu L, Yang Q, Guo W, Liaw PK, Dahmen KA, et al. Dislocation avalanche mechanism in slowly compressed high entropy alloy nanopillars. Commun Phys 2018;1:61.
[91] Zhang Q, Huang R, Zhang X, Cao T, Xue Y, Li X. Deformation mechanisms and remarkable strain hardening in single-crystalline high-entropy-alloy micropillars/nanopillars. Nano Lett 2021;21:3671–9.
[92] Weinberger CR, Cai W. The stability of Lomer–Cottrell jogs in nanopillars. Scr Mater 2011;64:529–32.
[93] Kumar A, Hauser FE, Dorn JE. Viscous drag on dislocations in aluminum at high strain rates. Acta Metall 1968;16:1189–97.
[94] Katagiri K, Pikuz T, Fang L, Albertazzi B, Egashira S, Inubushi Y, et al. Transonic dislocation propagation in diamond. Science 2023;382:69–72.
[95] Cao A, Wei Y, Mao SX. Alternating starvation of dislocations during plastic yielding in metallic nanowires. Scr Mater 2008;59:219–22.
[96] Zou Y, Ma H, Spolenak R. Ultrastrong ductile and stable high-entropy alloys at small scales. Nat Commun 2015;6:7748.